Coastal Engineering 208 (2026) 105009

Contents lists available at ScienceDirect

Coastal Engineering

journal homepage: www.elsevier.com/locate/coastaleng

# A CFD-Lagrangian model coupling for the transport, dispersion and accumulation of inertial non-spherical finite-size plastic debris in the surf zone

Paula Núñez [a,*], Alessandro Romano [b,a], Javier L. Lara [a], Gabriel Barajas [a], Raúl Medina [a], Giovanni Besio [c]

[a] IHCantabria - Instituto de Hidráulica Ambiental de la Universidad de Cantabria, Santander, Spain
[b] Roma Tre University, Department of Civil, Computer Science and Aeronautical Technologies Engineering, Rome 00146, Italy
[c] DICCA, University of Genoa, 1 Via Montallegro, I-16145 Genoa, Italy

ARTICLE INFO

*Keywords:*
Plastic debris
Particle inertia
Breaking waves
Surf zone
OpenFOAM®
Inertial Lagrangian modeling

ABSTRACT

Particle inertia is expected to play an important role in the transport, dispersion and accumulation of plastic debris driven by wave-breaking–induced currents and turbulence in the surf zone, particularly for large or dense materials. However, most numerical models still treat plastic debris as passive tracers and are rarely supported by systematic validation. This study proposes a one-way CFD–Lagrangian coupling framework for modeling wave-induced transport of inertial, non-spherical plastic debris spanning micro- to macro-sizes. Wave-induced hydrodynamics is modeled with OpenFOAM®, while debris trajectories are computed with a modified Maxey–Riley formulation that incorporates shape- and oscillatory-flow-dependent drag, added mass, stochastic dispersion, and a probabilistic beaching scheme. The methodology is calibrated and validated against 2DV wave-flume experiments on plastic-debris transport over a dissipative beach under regular spilling waves, covering 15 debris types with contrasting buoyancies/sizes/shapes/flexibilities across two release configurations. Numerical simulations reproduce the cross-shore evolution of concentrations and debris distributions observed in laboratory ($RMSE \approx 0.03$–$0.10\%$ and $R^2 = 0.70$–$0.99$, with slightly larger deviations for a few buoyant elements), confirming that transport and accumulation behaviors are strongly dependent on debris characteristics. Moreover, the Maxey–Riley coefficients calibrated with experimental data show systematic trends: oscillatory drag is inversely correlated with the Keulegan–Carpenter number; added mass depends on debris size and flexibility; and dispersion is strongly anisotropic and increases with turbulence. Overall, the proposed framework extends inertial Lagrangian-tracking models beyond small spherical particles and provides a physically based, computationally efficient tool for investigating plastic-debris dynamics in energetic coastal environments.

## 1. Introduction

Plastic debris constitutes more than 80% of the total marine litter entering the ocean, and its abundance has been rising steadily over recent decades (Derraik, 2002; Barnes et al., 2009; Villarrubia-Gómez et al., 2018). This increasing load affects not only habitats and ecosystems, but also key socioeconomic sectors such as fisheries and tourism, as well as human health (Derraik, 2002; Barnes et al., 2009; Galgani et al., 2015; Hardesty et al., 2017). Anticipating the transport and fate of plastic debris requires a solid understanding of the processes governing its transport, dispersion and accumulation. Such knowledge is essential to support effective monitoring, mitigation, and cleanup strategies (Schmaltz et al., 2020).

The transport and dispersion of plastic debris are influenced by both hydrodynamic factors and the intrinsic properties of the debris. Regarding hydrodynamic factors in the open ocean, large-scale currents and wind primarily govern transport, whereas in coastal regions, the interaction among waves, tides, and coastal currents dominates. As for debris properties, density, size, and shape are critical to understanding its response to flow variations, i.e., its inertial behavior. Small, light debris moves almost in synchrony with the flow, exhibiting weak inertia and behaving like a passive drifter, whereas larger, heavier debris deviates from flow streamlines and adapts more slowly to local hydrodynamics, showing strong inertial effects. The relative influence of hydrodynamic forcing and particle inertia can be expressed through

* Corresponding author.
*E-mail address:* nunezp@unican.es (P. Núñez).

https://doi.org/10.1016/j.coastaleng.2026.105009
Received 25 December 2025; Received in revised form 27 February 2026; Accepted 18 March 2026
Available online 19 March 2026

the Stokes number ($St$), defined as the ratio of the particle's characteristic response time ($\tau$) to the characteristic flow time ($\tau_f$). Stokes numbers of order one ($St = O(1)$) indicate relevant inertial effects, while values much smaller than one ($St \ll 1$) imply that hydrodynamic drag dominates.

Several approaches have been used in the literature to examine the transport of both non-inertial and inertial plastic debris across different spatial scales, from global to coastal regions. Some field studies of plastic debris trajectories have been conducted, but they remain relatively scarce (e.g., Olascoaga et al., 2020; Chen et al., 2022). In contrast, laboratory experiments and numerical modeling have been more widely employed.

Some laboratory experiments focus on non-breaking waves (Alsina et al., 2020; De Leo et al., 2021; Calvert et al., 2024), whereas most have been conducted in the surf zone (Forsberg et al., 2020; Kerpen et al., 2020; Guler et al., 2022; Larsen et al., 2023; Núñez et al., 2023b; Iuppa et al., 2024). Outside the surf zone, the transport of buoyant and non-buoyant debris is primarily governed by Stokes drift and bottom boundary layer effects, respectively. Within the surf zone, wave-breaking-induced currents and turbulence are the dominant forces. Turbulence generally reduces the characteristic flow time, leading to higher Stokes numbers ($St$) and making debris transport strongly dependent on the combined effects of inertial forces and turbulent fluctuations. Consequently, laboratory experiments provide valuable insights into particle dynamics and form a robust basis for the validation of numerical models.

Numerical modeling of plastic debris transport is commonly performed using Lagrangian tracking approaches, in which particles are advected by hydrodynamic flows. Two-dimensional horizontal (2DH) models typically treat debris as passive buoyant drifters and have been applied across a wide range of spatial scales, from global (Law et al., 2010; Lebreton et al., 2012; Van Sebille et al., 2012; Klink et al., 2022) to regional (Kako et al., 2011, 2014; Zambianchi et al., 2014, 2017; Declerck et al., 2019; Raimundo et al., 2020; Ruiz et al., 2022), and down to local estuarine and coastal environments (Núñez et al., 2019, 2020, 2021, 2025; Gorman et al., 2020; Ghosh et al., 2021). More recently, two-dimensional vertical (2DV) and three-dimensional (3D) models have been developed to investigate the transport of non-buoyant microplastics by incorporating gravitational effects through particle settling velocities (Jalón-Rojas et al., 2019; Li et al., 2024; Jalón-Rojas et al., 2025). Nevertheless, these approaches generally neglect inertial effects, limiting their ability to accurately represent the behavior of the heaviest microplastics as well as meso- and macroplastics commonly found in the marine environment (Zhang, 2017).

To date, few studies have explicitly addressed the inertial behavior of plastic debris using Lagrangian approaches based on simplified formulations of the Maxey–Riley equations (MRE). A limited number of numerical studies have applied MRE to buoyant spherical macroplastics in estuarine environments (Suara et al., 2020), while most others remain theoretical or consider simplified, idealized configurations, typically focusing on small spherical particles in two-dimensional vertical (2DV) flows driven by non-breaking gravity waves (Santamaria et al., 2013; Stocchino et al., 2019; DiBenedetto et al., 2022; De Leo and Stocchino, 2022). More recent work has extended these approaches to nearshore wave-breaking conditions (Rahmani and Stocchino, 2026), and initial insights into anisotropic microparticles have also been provided (DiBenedetto et al., 2018). Despite these advances, inertial models remain preliminary and largely unvalidated against experimental or field data. Laboratory findings suggest that the surf zone offers a particularly suitable environment to test these models, due to strong currents, turbulence, and flow variability that can amplify inertial effects.

Modeling plastic debris transport in the surf zone is particularly challenging, as Lagrangian tracking models require highly detailed hydrodynamic information that wave-averaged or depth-averaged models cannot capture. Although computationally demanding, computational fluid dynamics (CFD) methods, including Reynolds-Averaged Navier–Stokes (RANS) (Chella et al., 2015; Brown et al., 2016; Derakhti et al., 2016a,b; Devolder et al., 2018; Li et al., 2022), Large Eddy Simulation (LES) (Christensen and Deigaard, 2001; Christensen, 2006; Zhou et al., 2017), and Direct Numerical Simulation (DNS) (e.g., Deike et al., 2016; Wang et al., 2016), are capable of resolving these complex flows with high fidelity. Coupling Lagrangian tracking with CFD has mainly been applied to gases, aerosols, and pipe flows, with only a few studies targeting microplastic transport in the surf zone (e.g., Rahmani and Stocchino, 2026). While two-way approaches allow simultaneous simulation of hydrodynamics and particle transport, providing a more accurate representation of particle–fluid interactions (e.g., Eaton, 2009; Alletto and Breuer, 2012), they incur even higher computational costs and are rarely applicable over large spatial scales or long durations. One-way coupling offers a practical alternative by balancing computational efficiency with accurate representation of particle behavior (Berrouk et al., 2007; Dehbi, 2008; Tang et al., 2015; Di Paolo et al., 2021).

The state-of-the-art review indicates that most existing numerical models treat plastic debris as passive drifters. Only a few studies consider inertial dynamics, and these are mostly theoretical or rely on idealized configurations. While various CFD–Lagrangian coupling strategies have been developed in other contexts, applications to the inertial transport and dispersion of plastic debris in high-energy coastal environments such as surf zones remain extremely scarce, with only preliminary applications for spherical microplastics. Furthermore, the characterization of anisotropic micro-, meso-, and macroplastics remains limited, and experimental validation of these models is largely lacking.

This study proposed a novel one-way numerical coupling between the CFD model OpenFOAM® and a modified, specifically parameterized Lagrangian tracking model based on the MRE to simulate wave-induced transport of inertial, non-spherical plastic debris in the surf zone, from micro- to macro-sized particles. The Lagrangian model accounts for inertial effects, shape- and flow-dependent drag, gravity, stochastic dispersion, and beaching dynamics, representing debris retention in the swash zone. An effective velocity, incorporating interactions between particle geometry and local flow gradients, is included to capture flow nonuniformities, extending the MRE beyond the small-particle assumption and enabling a realistic representation of larger and irregular debris. The approach is calibrated and validated in a 2DV configuration against the experiments of Núñez et al. (2023b). The study's key novel contributions are: (i) adaptation of simplified MRE to model inertial, non-spherical, finite-size debris in turbulent coastal flows; (ii) development of an efficient one-way CFD–Lagrangian coupling combining a phase-resolving RANS–VOF solver with the MRE-based model and explicit boundary operators for bottom reflection, offshore removal, and probabilistic beaching, tailored for surf-zone transport, cross-shore sorting, and nearshore retention; and (iii) validation of the numerical model with explicit consideration of inertial forces on plastic debris.

This paper is structured as follows. Following this introduction, Section 2 provides an overview of the CFD and Lagrangian tracking models, along with the coupling strategy. Section 3 briefly describes the experimental data used for validation, while Section 4 details the computational setup. The main findings are presented in Section 5, and their implications are discussed in Section 6. Finally, Section 7 summarizes the key conclusions.

## 2. Numerical models and coupling strategy

### 2.1. Hydrodynamic model

In this study, wave-induced hydrodynamics is modeled using OpenFOAM® (Jasak, 1996), which provides a robust framework for coastal and ocean engineering applications, including wave-generation and absorption functionalities (Higuera et al., 2013a,b). Three-

dimensional Reynolds-Averaged Navier–Stokes (RANS) equations for two-phase flows are solved in combination with the Volume of Fluid (VOF) method to capture the free surface. The RANS equations rely on Reynolds decomposition, separating mean and fluctuating components of velocity and pressure for incompressible flow conditions. The governing equations express the conservation of mass and momentum, coupled with the VOF equation, as follows:

$$\nabla\cdot\mathbf{u} = 0, \tag{1}$$

$$\rho\left(\frac{\partial\mathbf{u}}{\partial t} + (\mathbf{u}\cdot\nabla)\mathbf{u}\right) = -\nabla p^* - (\mathbf{g}\cdot\mathbf{x})\nabla\rho - \mathbf{f}_\sigma + \nabla\cdot\left[\mu_{\text{eff}}\left(\nabla\mathbf{u} + (\nabla\mathbf{u})^\top\right)\right], \tag{2}$$

$$\frac{\partial\alpha}{\partial t} + \nabla\cdot(\alpha\,\mathbf{u}) + \nabla\cdot\left[\alpha(1-\alpha)\,\mathbf{u}_c\right] = 0. \tag{3}$$

where $\mathbf{u}$ denotes the ensemble-averaged velocity, $\mathbf{x}$ the Cartesian coordinates, and $\mathbf{g}$ the gravitational acceleration. The fluid density is represented by $\rho$, whereas the ensemble-average pressure in excess of hydrostatic is defined as $p^* = p - \rho\,\mathbf{g}\cdot\mathbf{x}$, where $p$ is the total pressure. The volume fraction $\alpha$ takes the value of 1 in the water phase and 0 in the air phase, serving as the indicator for the Volume of Fluid (VOF) function. The surface tension force per unit volume is $\mathbf{f}_\sigma = \sigma\,\kappa\,\nabla\alpha$, where $\sigma$ is the surface-tension coefficient and $\kappa$ is the interface curvature (Brackbill et al., 1992). The effective dynamic viscosity is the sum of the dynamic molecular viscosity and the turbulent viscosity ($\mu_{\text{eff}} = \mu + \rho\,\nu_t$), with $\nu_t$ provided by the turbulence closure model. The compression velocity is calculated as $\mathbf{u}_c = S\,\hat{\mathbf{n}}_\alpha$, with $\hat{\mathbf{n}}_\alpha = \nabla\alpha/\|\nabla\alpha\|$ and $S = \min\left(c_\alpha\|\mathbf{u}\|, U_{\max}\right)$, where the dimensionless compression coefficient $c_\alpha$ is assumed to be 1 (Weller, 2008; Marschall et al., 2012).

To close the RANS equations, OpenFOAM® includes several standard turbulence closure models, such as the $k$–$\varepsilon$, $k$–$\omega$, and $k$–$\omega$ SST formulations, with the enhancements proposed by Larsen and Fuhrman (2018). In this study, the non-standard Reynolds stress–$\omega$ (RSM–$\omega$) model of Li et al. (2022) is adopted for its improved representation of turbulence anisotropy and its ability to capture the dynamics of plunging and spilling breaking waves, consistent with the experimental benchmark in this study (Section 3).

### 2.2. Lagrangian tracking model

In this study, the transport of finite-sized, non-spherical particles is modeled using a Lagrangian tracking approach based on a modified and simplified version of the MRE. Following De Leo and Stocchino (2022), the model accounts for drag, gravity, added mass, and stochastic dispersion. The governing equations are given by:

$$\frac{\partial\mathbf{x}(t)}{\partial t} = \mathbf{u}^p(t) + \sqrt{2\mathbf{D}}\mathbf{R}(t), \tag{4}$$

$$\frac{\partial\mathbf{u}^p(t)}{\partial t} = \frac{\mathbf{u}_{\mathbf{eff}}(\mathbf{x},t) - \mathbf{u}^p(t)}{\tau} + (1-\beta)\mathbf{g} + \beta\frac{\partial\mathbf{u}_{\mathbf{eff}}(\mathbf{x},t)}{\partial t}. \tag{5}$$

Eq. (4) describes the evolution of the particle's position, where $\mathbf{x}(t)$ denotes the particle's center of gravity ($C_G$) and $\mathbf{u}^p(t)$ its velocity. Stochastic displacements are described through the random vector $\mathbf{R}(t)$ (zero mean, unit variance), representing a zeroth-order Markov process. This term, multiplied by the dispersion coefficient $\mathbf{D}$, provides a simplified random-walk approximation of the effects of unresolved subgrid-scale turbulent motions, thus remaining consistent with an effective diffusive closure (Drossinos and Reeks, 2005; Boi et al., 2015; De Leo and Stocchino, 2022). The implications of this diffusive assumption for nearshore plastic-debris transport are further discussed in Section 6.

Eq. (5) describes the particle's acceleration as the sum of three main contributions. The first term represents the particle's response to drag, where $\mathbf{u}_{\mathbf{eff}}(\mathbf{x},t)$ is the effective flow velocity acting on the particle and $\tau$ is the characteristic particle response time. The second and third terms account for gravitational acceleration and the local acceleration of the flow, respectively, both scaled by the added-mass parameter $\beta$, which captures the additional inertia transferred from the surrounding fluid to the particle.

A probabilistic beaching process is also included to represent debris retention in the swash zone. Local flow nonuniformities at the particle scale (Faxén-type effects) are not explicitly resolved, but are partially represented via an effective flow velocity evaluated at representative points on the particle surface. Other secondary terms in the full MRE, such as the Basset history term (viscous boundary-layer memory) and the Saffman lift force (shear-induced lateral forcing), are neglected because their contribution is expected to be small compared with the dominant inertial effects (Santamaria et al., 2013; DiBenedetto et al., 2018; Stocchino et al., 2019; De Leo and Stocchino, 2022). Particle–particle interactions are also neglected, consistent with the dilute suspension assumption, so that each particle evolves independently under the action of the flow and its own properties.

To summarize, this formulation builds on the approach of De Leo and Stocchino (2022), originally developed for spherical microplastics under sea waves. In this study, it has been extended and specifically calibrated against the experimental benchmark described in Section 3 to cover a broader range of debris characteristics, including micro- to macro-sized particles, non-spherical shapes, buoyancy variations, and pre- and post-breaking wave conditions. The following subsections detail each term in Eqs. (4)–(5), highlighting the key adaptations and the parameters subject to calibration, ensuring consistency across different debris types and turbulence intensities.

#### 2.2.1. Dispersion coefficient ($\mathbf{D}$)

The dispersion coefficient, $\mathbf{D}$, controls the amplitude of stochastic displacements in the particle trajectory equation, providing a simplified and synthetic representation of subgrid-scale turbulent dispersion (Drossinos and Reeks, 2005; Boi et al., 2015; Van Sebille et al., 2018; De Leo and Stocchino, 2022). In this study, $\mathbf{D}$ is treated as a calibration parameter and represented as anisotropic, with horizontal ($D_{\text{H}}$) and vertical ($D_{\text{V}}$) components. These components are calibrated separately for low-turbulence ($LT$, before wave breaking) and high-turbulence ($HT$, after wave breaking) regions, while enforcing the physically consistent constraint $r_D = D_{\text{V}}/D_{\text{H}} \leq 1$. Literature values for effective dispersion coefficients used in Lagrangian tracking models span orders of magnitude, from molecular diffusion, $10^{-6}$ m$^2$/s, to turbulent dispersion, $10^{-1}$ m$^2$/s (De Leo and Stocchino, 2022); this range is used to guide the calibration (Section 5.2).

#### 2.2.2. Effective velocity ($\mathbf{u}_{\mathbf{eff}}$)

In this study, the effective flow velocity driving each particle, $\mathbf{u}_{\mathbf{eff}}$, is defined to account for interactions between particle geometry and local flow gradients, rather than using the velocity evaluated at $C_G$. Although inspired by Faxén-type corrections, the formal Faxén terms are not included (Maxey and Riley, 1983; Gatignol, 1983). Instead, $\mathbf{u}_{\mathbf{eff}}$ is approximated by sampling the flow at a limited set of representative points on the particle surface and combining these values into an effective mean. The sampling strategy depends on particle shape, buoyancy, and the turbulence region (before vs after wave breaking), which together determine the preferred particle orientation. This approach captures the most relevant vertical variability while remaining computationally efficient.

In the $LT$ region, particle orientations are generally quasi-stable, nearly parallel to the bottom for non-buoyant particles or to the free surface for buoyant ones, thereby minimizing the projected cross-sectional area $A_c$ (DiBenedetto et al., 2018; Nayak et al., 2018). Accordingly, evaluating $\mathbf{u}_{\mathbf{eff}}$ at $C_G$ is considered sufficient. In the $HT$ region, where particle orientations can be more variable, $\mathbf{u}_{\mathbf{eff}}$ is computed as the average of the velocity at $C_G$ and at a second point vertically displaced by $\delta\cdot b$ along the intermediate particle axis $b$. The displacement is bounded so that the sampling point remains within the local water column (depth $h$) and represents an average particle tilt: upward for non-buoyant and downward for buoyant particles, reflecting their different effective immersion/tilt within the water column. The values of $\delta$ were obtained from preliminary numerical tests covering the debris

types considered (flat/cylindrical, compact/elongated, buoyant/non-buoyant; Section 3.2; Table 1). Specifically, $\delta$ was systematically varied within physically admissible bounds for each particle type. The adopted pair $(\delta_{NB}, \delta_B)$ was chosen as the one that best reproduces the temporal evolution of cross-shore concentrations. The resulting offsets are: $\delta_{NB} = +0.25$ for non-buoyant and $\delta_B = -0.90$ for buoyant particles, consistent with field evidence of orientations at higher turbulence levels (Nayak et al., 2018).

### 2.2.3. Characteristic particle response time ($\tau$)

The characteristic particle response time, $\tau$, indicates how quickly a particle adjusts its velocity to match that of the flow, with smaller $\tau$ corresponding to faster adaptation. In this study, the approach of Berrouk et al. (2007) is used to better capture fast and chaotic fluctuations associated with turbulence:

$$\tau = \frac{\rho_p}{\rho} \cdot \frac{4 d_p}{3 C_d |\mathbf{u_{eff}} - \mathbf{u}^p|}, \tag{6}$$

where $\rho_p$ is the particle density, $d_p$ the mean debris size (taken as the diameter of a volume-equivalent sphere), and $C_d$ the drag coefficient. The drag coefficient is expressed as:

$$C_d = C_d^u \cdot f_c, \tag{7}$$

where $C_d^u$ denotes the drag coefficient under uniform-flow conditions, and $f_c$ is a calibration factor accounting for oscillatory-flow effects, i.e., periodic acceleration and reversal that alter near-particle shear and wake dynamics, yielding an effective drag that deviates from steady uniform-flow predictions.

Beyond these oscillatory-flow corrections, the geometric representation of the particle also plays a relevant role. Although spherical drag formulations are commonly adopted for simplicity in microplastic transport studies (e.g. Stocchino et al., 2019; De Leo and Stocchino, 2022), this assumption becomes less appropriate for meso- and macroplastics, whose shape and orientation can markedly influence drag. In this study, $C_d^u$ is computed following Hölzer and Sommerfeld (2008), as that formulation explicitly accounts for particle shape and orientation across a wide range of non-spherical geometries:

$$C_d^u = \frac{8}{Re_p}\frac{1}{\sqrt{\Phi_\parallel}} + \frac{16}{Re_p}\frac{1}{\sqrt{\Phi}} + \frac{3}{\sqrt{Re_p}}\frac{1}{\Phi^{3/4}} + 0.4210^{0.4(-\log\Phi)^{0.2}}\frac{1}{\Phi_\perp}, \tag{8}$$

where $Re_p = d_p|\mathbf{u_{eff}} - \mathbf{u}^p|/\nu$ is the particle Reynolds number, with $\nu$ the kinematic viscosity of water; $\Phi = S_{eq}/S$ is the particle sphericity, with $S_{eq}$ the surface area of the volume-equivalent sphere and $S$ the actual particle surface area; $\Phi_\perp = A_{eq}/A_c$ is the crosswise sphericity, with $A_{eq}$ the cross-sectional area of the volume-equivalent sphere and $A_c$ the effective particle projected cross-sectional area normal to the flow direction; and $\Phi_\parallel = A_{eq}/(S/2 - A_l)$ is the lengthwise sphericity, where $A_l$ is the mean projected longitudinal area. This correlation $C_d^u$(8) is reported to account for shape and orientation effects over the full range of $Re_p$ up to the critical value, with no known applicability limits in terms of $\Phi$, $\Phi_\perp$, or $\Phi_\parallel$ (Hölzer and Sommerfeld, 2008). In the present simulations, $Re_p$ spans approximately $[0, 2\times10^4]$, remaining within this applicability range.

To estimate $A_c$, a reference maximum area is defined as $A_{\max} = a \cdot b$, with $a$ and $b$ the particle major and intermediate dimensions. In the $LT$ region, $A_c$ is taken as a reduced fraction of $A_{\max}$ to represent generally stable orientations that tend to minimize the area exposed to drag, while allowing for occasional deviations due to partial resuspension of non-buoyant debris near a sloping bottom or bending of buoyant debris driven by wave steepness and material flexibility (DiBenedetto et al., 2018; Nayak et al., 2018). For flat elements, the projected area normal to the flow is approximated as $A_c \approx |\sin\gamma| A_{\max}$, where $\gamma$ is the local inclination of the free surface (or bottom) relative to the horizontal. To avoid unrealistically small values under near-alignment with the flow (e.g., non-buoyant debris over locally horizontal bottoms), a lower bound is imposed: $A_c = \max\left(|\sin\gamma| A_{\max}, 0.01 A_{\max}\right)$. Furthermore, when a single representative value of the local inclination is required (e.g., to summarize the time-varying wave-induced slope relevant for buoyant particles aligned with the free surface), $\gamma$ is set to the maximum slope, $\gamma_{\max}$. For cylindrical debris, experimental observations indicate predominantly submerged transport. Non-buoyant cylinders are transported close to the bed, whereas buoyant cylinders are hollow and intermittently fill with water, resulting in a semi-submerged transport state close to the free surface. Consistent with this behavior, preliminary numerical tests show that a constant value $A_c \approx 0.85 A_{\max}$ provides a good representation and is only weakly sensitive to the local slope, since the effective drag is dominated by a major-axis-diameter length scale. In the $HT$ region, drag is assumed to act over the full $A_{\max}$. The longitudinal area, $A_l$, is computed as the mean of face-on and edge-on projections, namely $A_l = \frac{a(b+c)}{2}$ for flat elements (with $c$ the particle thickness) and $A_l = a \cdot b$ for cylindrical elements (Hölzer and Sommerfeld, 2008).

The factor $f_c$, used and calibrated in this study (Section 5.2), accounts for the effects of oscillatory flow on the drag coefficient. Since existing correlations for $C_d$ accounting for particle shape and orientation are typically derived for uniform flows (e.g., Hölzer and Sommerfeld, 2008), $f_c$ extends their applicability to oscillatory conditions. This factor is expected to depend primarily on the Keulegan–Carpenter number, $KC = VT/a$, where $V$ is the velocity amplitude, $T$ the oscillation period, and the characteristic particle length scale is defined by $a$ (Sarpkaya, 1986; Sánchez-González et al., 2011). The parameter $KC$ quantifies the ratio between the flow excursion over an oscillation cycle and the particle size: small $KC$ corresponds to particles large relative to the flow excursion (drag approaching quasi-uniform conditions), whereas large $KC$ indicates particles small relative to the excursion, promoting unsteady boundary-layer development, flow separation and vortex shedding, and complex velocity gradients that can modify (and often reduce) the effective drag.

Overall, pre-breaking motion is expected to be more strongly influenced by drag-mediated particle-flow coupling (through $C_d$ and $\tau$), whereas after breaking the contribution of turbulence-driven fluctuations to dispersion becomes comparatively more important and is primarily represented through the dispersion coefficient $\mathbf{D}$ (Section 2.2.1).

### 2.2.4. Added-mass parameter ($\beta$)

The added-mass parameter, $\beta$, quantifies the additional inertia acquired by a particle due to the fluid mass accelerated with it. In this study, $\beta$ is treated as a calibration parameter and initialized from the classical density-based expression for small spherical particles (e.g., Stocchino et al., 2019; De Leo and Stocchino, 2022), $\beta_0 = 3\rho/(2\rho_p + \rho)$. In the present context of finite-size and non-spherical particles, $\beta$ is used as an effective parameter that implicitly accounts for deviations from the ideal spherical assumption, including shape-, size-, and orientation-dependent particle–fluid coupling effects. The calibration is performed around the reference values provided by the classical formulation to reproduce the observed velocity response of different debris types, including compact, elongated, flat, and cylindrical shapes, whether buoyant or non-buoyant, across a wide range of particle sizes (Section 5.2).

### 2.2.5. Beaching probability ($P_b$)

To represent debris retention in the exposed (dry) area of the beach profile, a simple probabilistic approach is employed. Following the conceptual framework of previous studies (e.g., Lebreton et al., 2012; Critchell et al., 2015; Carlson et al., 2017; Cardoso and Caldeira, 2021), beaching is modeled as an irreversible process governed by a single calibrated probability, $P_b$, avoiding the need to explicitly resolve resuspension, which would require additional parameters that are currently poorly constrained (e.g., Mørk et al., 2026).

Within this probabilistic framework, each particle is assigned a binary state $X^n \in \{0, 1\}$ at time $t_n$, where $X^n = 0$ denotes a freely

moving particle and $X^n = 1$ denotes a beached (absorbing) state. The indicator $\chi^n_{\text{dry}} \in \{0, 1\}$ specifies whether the particle is located on an exposed area of the bottom at time $t_n$, with $\chi^n_{\text{dry}} = 1$ for dry conditions and $\chi^n_{\text{dry}} = 0$ when the particle is submerged. At each time step, a uniform random number $U^n \sim \mathcal{U}(0, 1)$ is drawn, and the particle state is updated as:

$$X^{n+1} = \begin{cases} 1, & \text{if } X^n = 0 \text{ and } U^n < P_b\, \chi^n_{\text{dry}}, \\ X^n, & \text{otherwise.} \end{cases} \tag{9}$$

Here, $P_b \in [0, 1]$ is treated as a calibration parameter fitted to reproduce experimentally observed retention rates (Section 5.2). Once a particle becomes beached, it remains permanently attached, with $P_b$ controlling the likelihood of stranding and the resulting accumulation of debris in the swash zone, i.e., the intermittently wet and dry portion of the beach driven by wave run-up and backwash.

### 2.3. Coupling strategy, numerical integration scheme, and boundary treatment

A one-way CFD-Lagrangian coupling strategy is adopted, in which particles are advected using hydrodynamic fields precomputed with a CFD model (OpenFOAM®) and no feedback from particles to the flow is considered. The Eulerian fields of velocity $\mathbf{u}(\mathbf{x}, t)$ and turbulence quantities (e.g., turbulent kinetic energy and dissipation) drive particle-scale advection and dispersion. Flow variables are linearly interpolated in space and time along particle trajectories and evaluated at representative points on the particle surface according to the effective-velocity formulation (Section 2.2.2). Turbulence intensity controls the dispersion tensor $\mathbf{D}$ (Section 2.2.1) and also affects the drag coefficient through its influence on particle orientation and projected area (Section 2.2.3).

Eqs. (4)–(5) are integrated using an operator-splitting scheme with a time step $\Delta t$. Over each $\Delta t$, the deterministic terms are first advanced with a fourth-order Runge–Kutta (RK4) method. This conducts to an intermediate deterministic state $(\mathbf{x}^{n+1}_{\text{det}}, \mathbf{u}^{n+1}_p)$. Stochastic dispersion due to unresolved turbulence is then incorporated at the position level via an additive Brownian increment. Since dispersion is represented as anisotropic with horizontal and vertical components, $\mathbf{D}$ is applied component-wise (diagonal in the chosen coordinates), and the update reads:

$$\mathbf{x}^{n+1} = \mathbf{x}^{n+1}_{\text{det}} + \sqrt{2\,\mathbf{D}\,\Delta t}\,\boldsymbol{\xi}^n, \qquad \boldsymbol{\xi}^n \in \mathbb{R}^d, \quad \boldsymbol{\xi}^n \sim \mathcal{N}(\mathbf{0}, \mathbf{I}_d), \tag{10}$$

where $\mathbf{I}_d$ is the $d \times d$ identity matrix and $\boldsymbol{\xi}^n$ has independent components with zero mean and unit variance. This discrete update can be interpreted as a time-discretized approximation of the continuous stochastic differential equation:

$$\mathrm{d}\mathbf{x} = \mathbf{u}_p\,\mathrm{d}t + \sqrt{2\,\mathbf{D}}\,\mathrm{d}\mathbf{W}_t, \tag{11}$$

where $\mathbf{W}_t$ denotes a standard Wiener process. By construction, the componentwise dispersive scaling is preserved:

$$\mathrm{Var}(\Delta x_i) = 2\,D_i\,\Delta t, \quad i = 1, \ldots, d. \tag{12}$$

As the stochastic displacement acts only on position (additive noise), the particle velocity used as the initial condition in the next deterministic RK4 step remains unchanged ($\mathbf{u}^{n+1}_p$).

Boundary conditions are explicitly treated within the numerical scheme to ensure consistent particle–boundary interactions. Particles are confined within the fluid region through impermeable reflection conditions at the bottom and free surface. Impermeable reflection is implemented as a no-penetration condition at both the bed and the free surface. At each time step, if a particle crosses the bed ($z^p < z_b$) or the free surface ($z^p > \eta$), its vertical position is reflected back into the fluid domain across the corresponding boundary, while the tangential velocity components remain unchanged. When advected into the swash zone, particles may become beached according to the probabilistic model (Section 2.2.5), whereas those crossing the offshore boundary are removed from the computational domain. This treatment preserves both the physical realism of near-boundary dynamics and the numerical stability of the Lagrangian solver.

## 3. Experimental benchmark

### 3.1. Experimental setup

As stated, the experimental data by Núñez et al. (2023b) are used as a benchmark for calibration and validation. A brief description of the experimental dataset is provided here, while the readers are referred to the original publication for further details. This dataset refers to 2DV wave-flume experiments of plastic-debris transport over a dissipative beach under regular and irregular waves, covering 15 plastic materials (P$i$, $i$ = 1, 2, …, 15) with contrasting sizes, shapes, and buoyancies, across two initial-release configurations. The experiments were carried out in a 20.6 m long, 0.6 m wide, and 0.75 m high wave flume with a fixed dissipative beach profile (8.6 m constant-depth section, $h = 0.45$ m, followed by a 1:20 methacrylate slope; Fig. 1a).

The study focuses on spilling breaking waves generated under two regular-wave conditions, defined by wave height ($H$) and wave period ($T$): ($W1$: $H = 0.18$ m, $T = 1.5$ s; $W2$: $H = 0.10$ m, $T = 2.0$ s). The corresponding wave kinematics are prescribed using second-order Stokes (Stokes II) theory. In addition, an irregular-wave condition ($W3$) is defined by a significant spectral wave height ($H_{m0} = 0.10$ m), peak period ($T_p = 1.5$ s), and a TMA (Texel-Marsen-Arsloe) spectrum, consisting of 1000 waves in shallow water. Free-surface elevation and wave-induced currents are available at the wave gauge (WG) and acoustic Doppler velocimeter (ADV) locations (Fig. 1a).

For model calibration and validation, experiments under conditions $W2$ and $W1$ are reproduced, respectively, as focusing on regular waves provides a simplified yet representative framework for nearshore dynamics, reduces uncertainty associated with irregular forcing, and enables consistent comparison with experimental observations. This approach therefore establishes a well-defined calibration–validation protocol and serves as an initial step toward testing the framework under more complex coastal conditions.

For reference, the cross-shore zones used in the analysis are defined based on wave transformation stages, including offshore, shoaling, breaking, surf, and swash regions. The boundaries are measured from the paddle: for $W2$, the offshore–shoaling, shoaling–breaking, breaking–surf, and surf–swash transitions are located at $x = 8.6$, 14.3, 15.3, and 16.7 m, respectively. For $W1$, the corresponding boundaries are $x = 8.6$, 11.6, 13.5, and 16.7 m.

### 3.2. Plastic materials (Pi)

The analyzed P$i$ span micro- to macroplastics and cover a broad range of shapes, including flat and cylindrical, as well as compact and elongated forms. The P$i$ dataset includes both buoyant and non-buoyant debris with different degrees of flexibility. These characteristics affect the hydrodynamic response in water, including drag, added mass, dispersion, and beaching. Table 1 summarizes the main properties and introduces an operational flexibility class ($F$), defined from particle dimensions ($a$, $b$, and $c$, denoting the major axis, intermediate axis, and thickness, respectively).

$F$ is defined in the present work as an operational descriptor to account for the tendency of different plastic items to bend and reorient under wave forcing. This influences their projected area and near-surface alignment. The classification relies on simple geometric proxies (thickness $c$ and aspect ratio) available for all items in the dataset. Thresholds (e.g., $c = 0.1$ mm) are heuristic and were selected to distinguish thin-film items that are readily deformable in water from thicker sheets that tend to retain their shape, while maintaining a minimal number of classes. Compact flat elements with thickness $c > 0.1$ mm

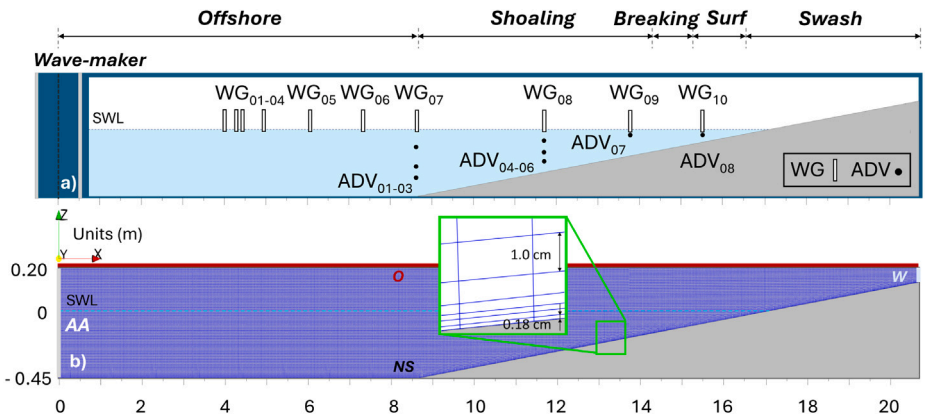


**Fig. 1.** Experimental and numerical setups: (a) locations of wave gauges (WGs) and Acoustic Doppler Velocimeters (ADVs) across the offshore, shoaling, breaking, surf, and swash zones for condition $W2$ (adapted from Núñez et al., 2023b); (b) numerical grid with $\Delta x = 0.02$ m, $\Delta z = 0.01$ m, six surface layers, a vertical expansion ratio 1:4, and boundary conditions: active absorption ($AA$), wall ($W$), no-slip ($NS$), and open ($O$).

**Table 1**
Physical properties of the benchmark plastic materials ($Pi$): representative Shape class, sphericity ($\Phi$), flexibility ($F$), density ($\rho_P$), major ($a$) and intermediate ($b$) axes, thickness ($c$), and the reference particle response time ($\tau_0$), estimated as $\tau_0 = d_p^2/(12\beta_0\nu)$. Adapted from Núñez et al. (2023b).

| Pi | Shape | $\Phi$ | $F$ | $\rho_p$ (kg m$^{-3}$) | $a$ (mm) | $b$ (mm) | $c$ (mm) | $\tau_0$ (s) |
|---|---|---|---|---|---|---|---|---|
| P1 | Sheet | 0.223 | Null | 1340 | 4.9 | 4.9 | 0.15 | 0.2 |
| P2 | Sheet | 0.117 | Null | 1340 | 13.6 | 13.6 | 0.15 | 0.9 |
| P3 | Sheet | 0.044 | Null | 1340 | 75.0 | 50.0 | 0.15 | 6.0 |
| P4 | Flat strip | 0.082 | Low | 1340 | 108.0 | 4.9 | 0.15 | 2.0 |
| P5 | Flat strip | 0.071 | Mid | 1340 | 162.5 | 4.9 | 0.15 | 2.0 |
| P6 | Flat strip | 0.057 | High | 1340 | 325.0 | 4.9 | 0.15 | 3.5 |
| P8 | Fiber bundle | 0.286 | High | 1020 | 180.0 | 2.0 | 2.00 | 0.7 |
| P9 | Sheet | 0.019 | Mid | 910 | 210.0 | 148.5 | 0.12 | 17.0 |
| P10 | Sheet | 0.013 | High | 910 | 210.0 | 148.5 | 0.07 | 12.0 |
| P11 | Sheet | 0.025 | High | 910 | 80.0 | 55.0 | 0.07 | 3.0 |
| P12 | Sheet | 0.138 | High | 910 | 4.9 | 4.9 | 0.07 | 0.1 |
| P14 | Cylindrical tube | 0.376 | Null | 900 | 108.0 | 3.0 | 0.20 | 1.0 |
| P15 | Cylindrical tube | 0.502 | Null | 900 | 5.0 | 3.0 | 0.20 | 0.2 |
| P7 | Nonwoven sheet | 0.121 | Low | 380 | 175.0 | 95.0 | 1.50 | 40.0 |
| P13 | Nonwoven sheet | 0.151 | Low | 380 | 95.0 | 87.5 | 1.50 | 25.0 |

(P1–P3) are classified as rigid. Elongated pieces of similar thickness (P4) are assigned moderate flexibility, whereas longer strips (P5–P6) and filaments (P8) are more flexible due to their larger aspect ratio or fibrous structure. For large sheets (P9–P12), flexibility depends on thickness: thicker sheets ($c > 0.1$ mm; P9) are moderately flexible, while thinner ones ($c < 0.1$ mm; P10–P12) are highly deformable. P14 and P15 are rigid ($c = 0.2$ mm). Face masks (P7, P13) exhibit low flexibility: their nonwoven texture provides some malleability, but their thickness ($c = 1.5$ mm) limits deformation in water.

### 3.3. Experimental methodology

In the experimental benchmark, releases were defined by their initial spatial configuration rather than by prescribing a fixed number of items per debris type. Accordingly, P$i$ were released under two initial configurations: (i) concentrated in the swash zone ($IC_{\mathrm{SW}}$), with plastic debris distributed in rectangular areas spanning the full width of the flume and 0.3 m along its length, centering approximately 17.3 m from the paddle on the initially dry bottom and (ii) uniformly distributed along the flume ($IC_{\mathrm{UD}}$), with debris arranged to approximate a uniform cross-shore distribution on the surface and on the bottom for buoyant and non-buoyant debris, respectively. For each run, debris was placed in the flume before wave generation and allowed to evolve under wave forcing for 18 min until reaching a quasi-steady distribution.

To quantify the debris distribution, the concentration in each zone $k$ (offshore, shoaling, breaking, surf, and swash) at time $t$ was defined as the percentage of the total detected debris area located within that zone, i.e., $C_k^{\exp}(t) = \frac{A_k(t)}{\sum_k A_k(t)} 100$, where $A_k(t)$ denotes the debris-covered area in zone $k$ obtained from plan-view video image analysis. The reliability of this area-based quantification and the potential influence of debris overlapping were independently assessed through weight measurements, confirming that the detected area provides a consistent proxy for debris quantity.

### 3.4. Inertia and Stokes number of Pi

As outlined above, the Stokes number, $St = \tau/\tau_f$, quantifies the importance of particle inertia relative to hydrodynamic forcing. A reference estimate of the particle response time, $\tau_0$, is adopted here only as a first-order, descriptive indicator of the overall inertial response of each P*i*, while neglecting relative-velocity effects that vary in time under wave forcing (Stocchino et al., 2019; De Leo and Stocchino, 2022). The Lagrangian model instead uses the time-dependent response time $\tau$ defined in Section 2.2.3, which depends on the instantaneous relative velocity. Accordingly, the reference particle response time is estimated as $\tau_0 = d_p^2/(12\beta_0\nu)$, where $\beta_0$ is the density-based reference value (Section 2.2.4).

The resulting characteristic response times $\tau_0$ cover a wide range (Table 1): small materials (e.g., P1, P12, P15) have $\tau_0 \leq 0.3$ s; intermediate debris (P2, P8, P14) exhibit $\tau_0 \approx 1$ s; larger materials (P3-P6, P11) have $\tau_0 \in [2, 6]$ s; wider sheets (P9-P10) reach up to $\tau_0 \approx 17$ s; and the most voluminous particles (P7, P13) reach $\tau_0 \approx 40$ s. Assuming characteristic flow times of $\tau_f = 2$ s (wave period for $W2$) and $\tau_f = 1.5$ s (wave period for $W1$), the corresponding Stokes numbers span over two orders of magnitude. Most P*i* have $St \geq 1$, indicating strong inertia where trajectories deviate notably from the flow, while smaller or intermediate materials ($0.05 \leq St \leq 0.7$) largely follow the fluid motion with a slight phase lag.

Overall, these estimates indicate that, in addition to turbulence in the wave-breaking zone, inertial effects can significantly influence P*i* transport. This supports the use of the Lagrangian tracking model described in Section 2.2, in which drag, added mass, and stochastic dispersion are adjusted to reproduce the inertial response across the observed range of plastic debris.

## 4. Modeling setup

### 4.1. Hydrodynamic model

The experimental setup of Núñez et al. (2023b) (Section 3.1) is reproduced by building a numerical 2DV wave flume. The computational grid consists of 0.09M cells with resolutions of $\Delta x = 0.02$ m and $\Delta z = 0.01$ m in the horizontal and vertical directions, respectively. This resolution captures the main wave-breaking hydrodynamics while conforming to the underlying geometry. To better resolve boundary-layer processes, which are critical for the transport of non-buoyant debris, six refined vertical layers with an expansion ratio of 1:4 are added near the bottom (Fig. 1b). Sensitivity analyses on grid resolution, boundary-layer configuration, and model dimensionality guided the selection of the final setup Appendix, which was chosen based on agreement with measured free-surface elevations and wave-induced currents.

Consistent with the experiments, the water depth is set to $h = 0.45$ m. The regular-wave conditions $W2$ and $W1$ (Section 3.1) are simulated using Stokes II theory. Active absorption is applied at the inlet (left boundary), while the right boundary is treated as a wall. The bottom boundary is no-slip and impermeable, the top boundary is open, and the lateral boundaries are set as empty, enforcing 2D flow. Turbulence generated by spilling breaking waves is modeled using the RSM-$\omega$ closure of Li et al. (2022). The simulation duration for both $W1$ and $W2$ matches the laboratory runs (18 min). Throughout the simulations, free-surface elevation, wave-induced currents, and turbulence quantities (e.g., $k$ and $\nu_t$) are recorded at 10 Hz ($\Delta t = 0.1$ s), providing the input fields for the Lagrangian tracking model and the dispersion parameterization. The simulations are performed using a Intel® Core™ i7-7700K CPU 4.20 GHz CPU unit, 32 GB RAM desktop computer, executed on a single CPU core (serial execution), and require approximately 3 days of wall clock time.

### 4.2. Lagrangian tracking model

The Lagrangian tracking model is driven by the velocity and turbulence fields obtained from the CFD simulations via one-way coupling. The velocity field provides the hydrodynamic forcing entering the particle equations, while turbulence-related quantities inform the Lagrangian parameterizations. The fluid density is set to $\rho = 1000$ kg/m$^3$.

Breaking-induced mixing effects are incorporated using the non-dimensional flow-kinematics indicator proposed by Larsen and Fuhrman (2018). The period-averaged ratio $\langle p_\Omega \rangle / \langle p_0 \rangle$ is computed, where $p_0$ and $p_\Omega$ are invariants of the mean strain-rate and rotation tensors obtained from the resolved velocity gradients. The averaging $\langle \cdot \rangle$ is performed over fifty wave periods ($50T$) to reduce short-term fluctuations. Regions with $\langle p_\Omega \rangle / \langle p_0 \rangle \leq \lambda_2$ (with $\lambda_2 = 0.05$, a practical choice in discretized computations) are classified as nearly-potential flow, whereas larger values indicate non-potential (rotational/sheared) flow. The breaking-affected transport region ($HT$) is defined by $\langle p_\Omega \rangle / \langle p_0 \rangle \geq 0.8$ (Fig. 2f), while the low-perturbation region ($LT$) corresponds to the complementary area (including nearly-potential and weakly non-potential regions). Sensitivity tests varying the $HT$-threshold between 0.7 and 0.9 showed negligible changes in the $LT/HT$ spatial partition and in the resulting dispersion patterns. This $LT/HT$ classification is then used to modulate stochastic dispersion (Section 2.2.1) and particle-orientation assumptions, which affect the effective velocity (Section 2.2.2) and the projected particle areas used to define the drag coefficient (Section 2.2.3).

Within this flow-based framework, each particle is assigned a set of physical and geometric descriptors. Each particle is characterized by its density $\rho_p$ (Table 1), equivalent-sphere diameter $d_p$, sphericity $\Phi$, and the orientation-dependent sphericities $\Phi_\perp$ and $\Phi_\parallel$, computed from the projected areas implied by the $LT/HT$ orientation assumptions (Section 2.2.3). Several model parameters are treated as calibration variables: the oscillatory-flow drag correction factor $f_c$, the added-mass coefficient $\beta$, the horizontal and vertical dispersion coefficients before and after wave breaking ($D_{\mathrm{H}}^{\mathrm{LT}}$, $D_{\mathrm{V}}^{\mathrm{LT}}$, $D_{\mathrm{H}}^{\mathrm{HT}}$, $D_{\mathrm{V}}^{\mathrm{HT}}$), and the beaching probability $P_b$. Parameter ranges are selected based on reference estimates and preliminary sensitivity tests. $f_c$ is constrained to [0,1] because it scales the uniform-flow drag coefficient: $f_c = 1$ corresponds to no oscillatory correction, whereas $f_c < 1$ represents a reduced effective drag under oscillatory flow. The upper bound is a conservative choice that avoids compensating for other processes (e.g., breaking-induced turbulence/mixing) by artificially increasing drag beyond the uniform-flow formulation. $\beta$ is explored around $\beta_0$, using separate intervals for non-buoyant debris ($\beta < 1$) and buoyant debris ($\beta > 1$). Dispersion coefficients are varied over multiple orders of magnitude, from values representative of molecular diffusion ($10^{-6}$ m$^2$/s) to turbulent dispersion ($10^{-1}$ m$^2$/s), with separate ranges for low- and high-turbulence regions to account for the strong increase in wave-breaking-driven mixing across the breaking transition. The specific ranges chosen before and after breaking correspond to these orders of magnitude and are consistent with values commonly adopted in wave-resolving Lagrangian applications (e.g., De Leo and Stocchino, 2022; Jalón-Rojas et al., 2025). Finally, $P_b$ is explored over its admissible range [0,1]. The final bounds listed in Table 2 ensure that the explored ranges bracket the observed variability.

The numerical settings are consistent with the experimental benchmark, and simulations are run over the same time window as the laboratory tests. The number of particles is set to $N = 1000$, consistent with values commonly adopted in previous studies (e.g., Díaz et al., 2008; Núñez et al., 2019). This choice is supported by preliminary sensitivity analyses with $N = 500$, 1000, and 2000 particles, which indicate that $N = 1000$ provides a suitable compromise between accuracy and computational cost. The integration time step is set to $\Delta t = 0.1$ s, more than one order of magnitude smaller than $\tau$ for most P*i* and comparable to $\tau$ for the smallest ones (P1, P12, and P15), ensuring

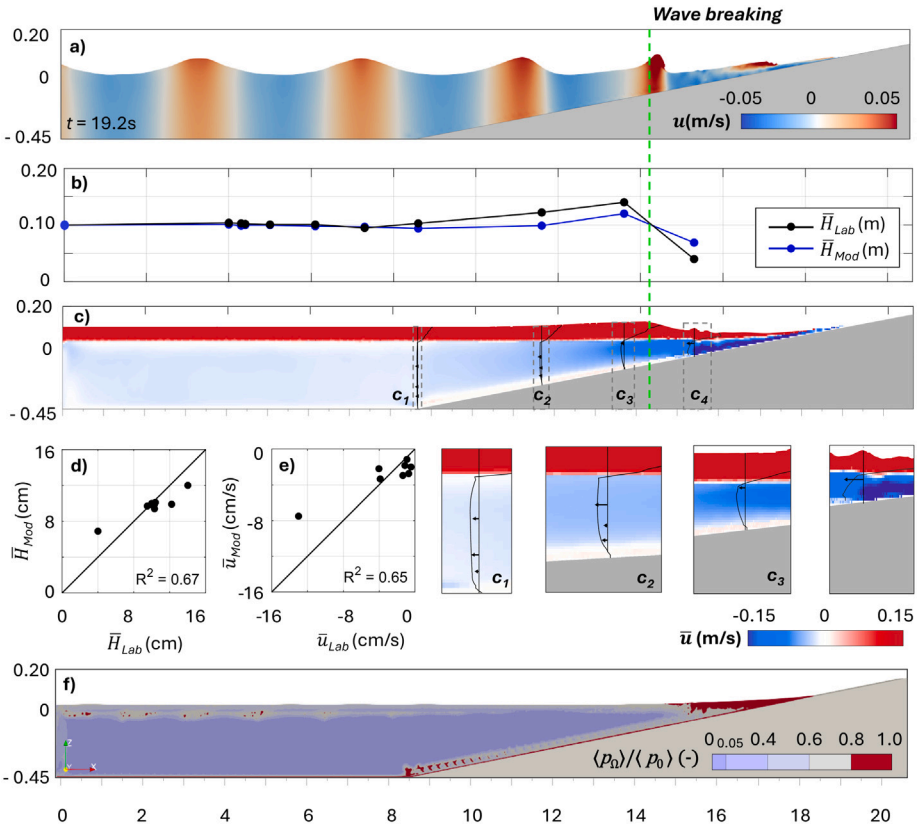


**Fig. 2.** Hydrodynamic and turbulence fields for $W2$: (a) spatial distribution of time-averaged wave height from the model ($\bar{H}_{Mod}$) and laboratory measurements ($\bar{H}_{Lab}$); (b) instantaneous horizontal velocity ($u$) at $t$ = 19.2 s; (c) time-averaged horizontal currents ($\bar{u}$) with vertical profiles (model results shown as red/blue shaded areas, numerical profiles as black lines, laboratory measurements as black arrows); (d) comparison of $\bar{H}_{Mod}$ vs $\bar{H}_{Lab}$; (e) comparison of $\bar{u}_{Mod}$ vs $\bar{u}_{Lab}$; and (f) spatial distribution of the non-dimensional flow-kinematics ratio $\langle p_\Omega \rangle / \langle p_0 \rangle$, used to delineate breaking-affected transport regions ($HT$; $\langle p_\Omega \rangle / \langle p_0 \rangle > 0.8$) from low-perturbation ($LT$) conditions.

**Table 2**
Parameter ranges used for calibration of the Lagrangian tracking model.

| Parameter | Description | Range tested |
|---|---|---|
| $f_c$ | Correction factor of $C_d$ for oscillatory flow (-) | [0, 1.00] |
| $\beta$ | Added-mass coefficient (non-buoyant/buoyant) (-) | [0.70, 0.99]/[1.01, 1.40] |
| $D_H^{LT}$ | Horizontal dispersion before wave breaking (m$^2$/s) | [1.0e−6, 1.5e−2] |
| $D_V^{LT}$ | Vertical dispersion before wave breaking (m$^2$/s) | [1.0e−7, 1.0e−4] |
| $D_H^{HT}$ | Horizontal dispersion after wave breaking (m$^2$/s) | [5.0e−4, 3.0e−2] |
| $D_V^{HT}$ | Vertical dispersion after wave breaking (m$^2$/s) | [2.0e−4, 2.0e−2] |
| $P_b$ | Beaching probability (-) | [0, 1.0] |

numerical stability and an adequate resolution of the particle inertial response, in line with Stocchino et al. (2019). Particle positions are stored every 0.1s, allowing the computation of particle concentrations $C(t)$ to be estimated along the beach profile for each P$i$ and compared with the experimental observations used for calibration.

The same initial-release configurations tested in the laboratory ($IC_{SW}$ and $IC_{UD}$) are adopted in the numerical simulations. For $IC_{SW}$, particles are distributed in the swash zone with an ensemble centroid at $x_0$ = 17.3 m and a total release length of 0.30 m (i.e., extending ±0.15 m about $x_0$). For $IC_{UD}$, particles are uniformly distributed along the flume over $x \in$ [0.0, 16.6]m. The initial vertical position is set at the bottom elevation for non-buoyant debris and at the free surface for buoyant debris, with particle release at $t$ = 0 (start of each run). The debris concentration in zone $k$ is defined as the fraction of particles located in that zone, $N_k(t)$, relative to the total number of released particles, $N$, i.e., $C_k^{num}(t) = \frac{N_k(t)}{N} 100$. Although the experimental definition is based on area fraction and the numerical one on particle fraction, the two measures are directly comparable because particles within each $Pi$ class are geometrically identical, making area and particle fractions proportional indicators of debris redistribution.

The simulations are performed using a Intel® Core™ i7-7700K CPU 4.20 GHz CPU unit, 32 GB RAM desktop computer, executed on a single CPU core (serial execution), and require approximately 30 min of wall clock, demonstrating the computational efficiency of the model.

### 4.3. Statistical evaluation metrics

Model performance is evaluated using a set of statistical indicators applied to both hydrodynamic and debris-transport quantities. The metrics are computed from modeled and observed time series, enabling a direct quantitative comparison of their temporal evolution.

For hydrodynamic quantities (free-surface elevation and velocity), the bias ($BIAS$), root-mean-square error ($RMSE$), skill score ($Skill$), and squared Pearson correlation coefficient ($R^2$) are computed following standard formulations (e.g., Willmott, 1981; Legates and McCabe, 1999). $BIAS$ measures systematic deviations, $RMSE$ the overall error

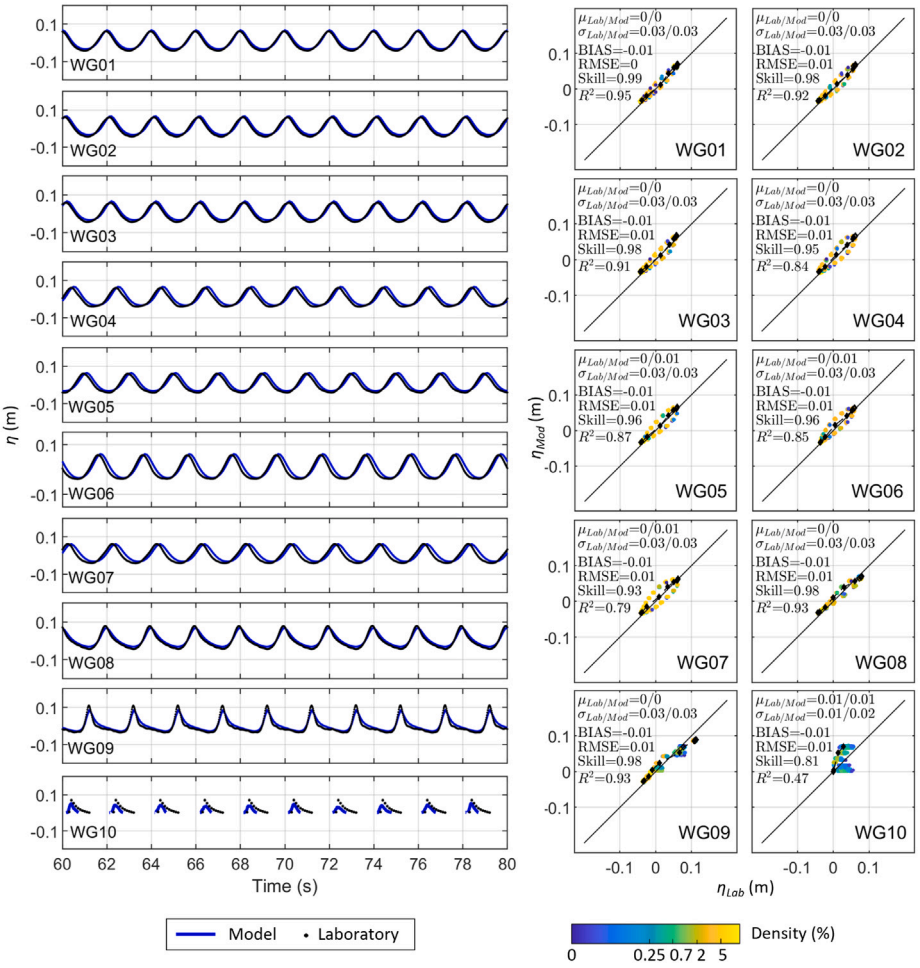


**Fig. 3.** Validation of free-surface elevation ($\eta$) under $W2$. Time series at each WG over 60–80 s (left panels) and scatter plots of numerical ($\eta_{\mathrm{Mod}}$) vs laboratory measurements ($\eta_{\mathrm{Lab}}$) over the full 18-min simulation (right panels), colored by point density, with the 1:1 line and relevant statistical metrics.

magnitude, $Skill$ the normalized agreement, and $R^2$ the strength of linear association between modeled and observed time series.

For debris-transport quantities, the evaluation focuses on the temporal evolution of debris concentrations across the offshore, shoaling, breaking, surf, and swash zones. Performance is assessed using $RMSE$ (primary metric), mean absolute error ($MAE$), $Skill$, and $R^2$. In addition, the statistical significance of the Pearson correlation is evaluated through its associated $p$-value (with $p < 0.05$ indicating significance). $MAE$ complements $RMSE$ by being less sensitive to outliers. A separate $BIAS$ metric is not reported for concentrations, as the analysis emphasizes relative agreement and error magnitude across zones and time, captured by $RMSE$ and $MAE$. $Skill$, $R^2$, and the $p$-value provide complementary information on agreement.

The performance statistics are computed using procedures tailored to each component of the modeling framework. For hydrodynamic quantities, model outputs are stored every 0.1 s, while experimental records are available every 0.02 s; comparisons are therefore performed at the coarser temporal resolution of 0.1 s. The initial 18 s ($\approx 9T$) are excluded as a warming period, and only the quasi-steady wave regime is analyzed. Comparisons are performed at the WG and ADV locations (Fig. 1a). For debris-transport quantities, metrics are computed over a window of $4T$, consistent with the experimental observations. The reported values are averaged across both initial conditions ($IC_{\mathrm{SW}}$, $IC_{\mathrm{UD}}$), providing an integrated measure of model performance.

## 5. Results

### 5.1. Wave breaking hydrodynamics

Hydrodynamic results from the numerical wave-flume model are presented alongside laboratory measurements in detail for $W2$ (Figs. 2, 3, and 4). Fig. 5 then provides an independent summary of the same validation metrics for $W1$.

For $W2$, an instantaneous horizontal-velocity field at $t = 19.2$ s shows that wave breaking occurs at approximately $x = 14.3$ m from the paddle, consistent with the experimental observations (Fig. 2a). The wave-breaking hydrodynamics are then quantified using time-averaged fields (computed over $50T$) of wave height, currents, and turbulence intensity, and complemented by a detailed comparison of free-surface elevation and velocity time series.

The comparison between modeled and measured average wave heights ($\bar{H}$; Figs. 2b, d), shows overall good agreement ($R^2 = 0.67$). However, the model slightly underestimates wave height before breaking (mean residuals of 0.008 m) and overestimates it after breaking by about 0.027 m. Since the comparison involves only 10 wave gauges, the higher discrepancies after wave breaking have a strong influence on the cross-shore correlation, despite the good agreement observed in the free-surface time series (Fig. 3).

Regarding the time-averaged horizontal velocity field ($\bar{u}$), the model reproduces the characteristic circulation pattern induced by wave breaking, featuring onshore currents near the surface and

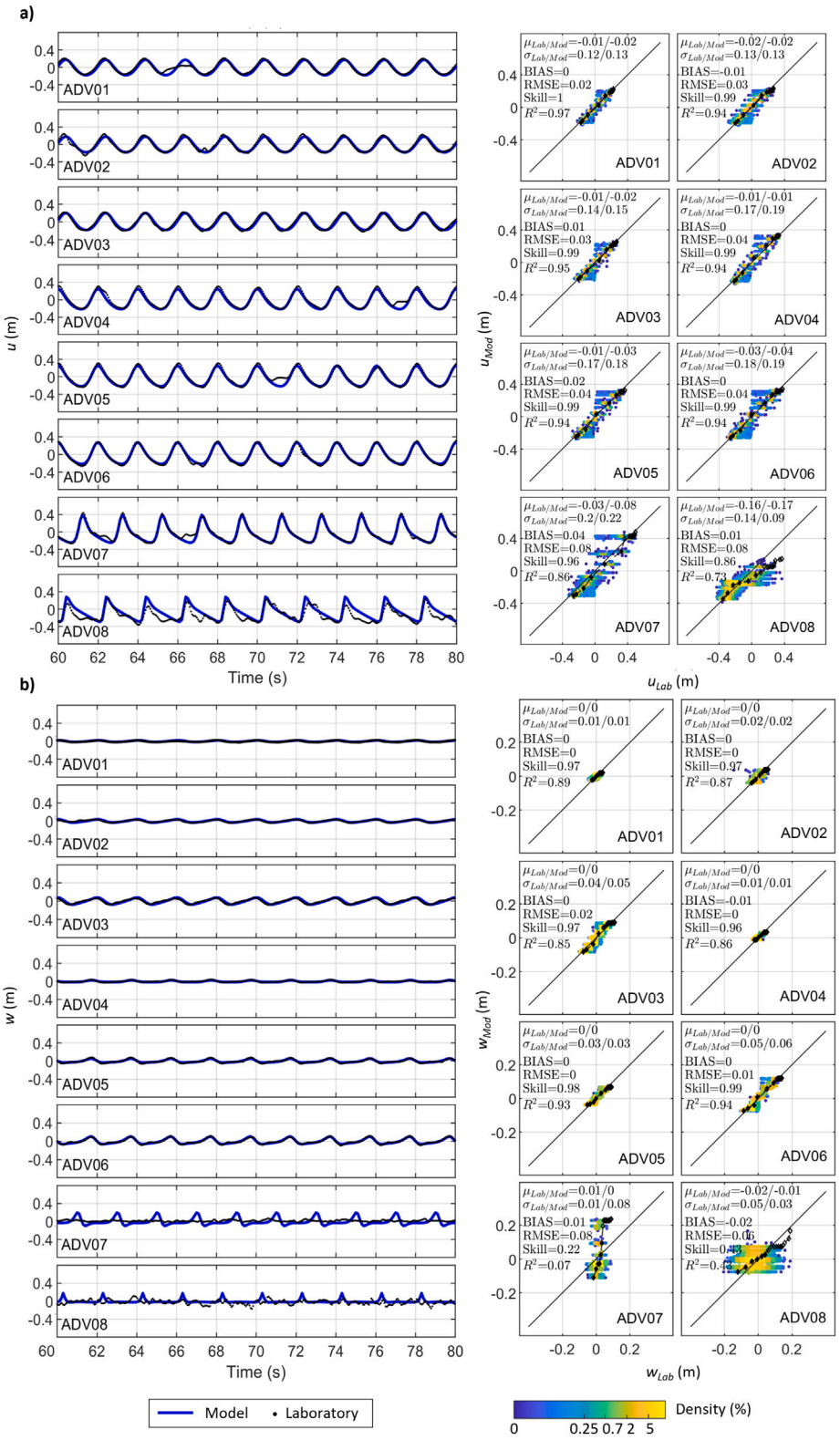


**Fig. 4.** Validation of wave-induced velocities at each ADV under $W2$: (a) horizontal velocity $u$, and (b) vertical velocity $w$. Left panels show time series between $t$ = 60 and 80 s, while right panels show scatter plots over the full 18-min simulation, colored by point density, including the 1:1 line and relevant statistical metrics.

offshore-directed return flow (undertow) close to the bed (Fig. 2c). A nearshore flow detachment zone develops around the breaking point, which is expected to influence the transport and dispersion of non-buoyant debris. The correlation between modeled and measured mean currents is $R^2$ = 0.65, with the main differences occurring in the post-breaking region, where the model overestimates the mean velocity by approximately 0.07 m/s (Fig. 2e). Vertical velocity profiles at cross-shore locations $c_1$-$c_4$ further illustrate this circulation pattern.

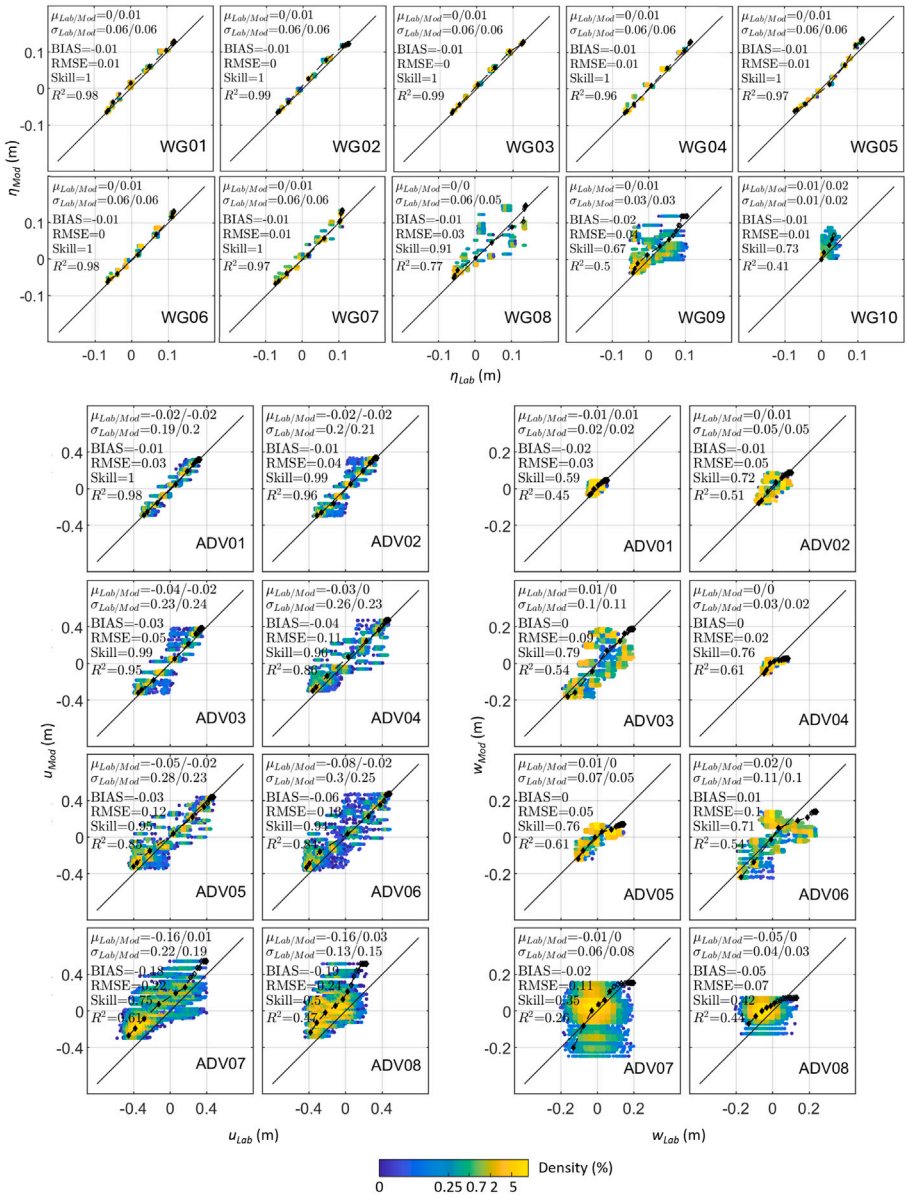


**Fig. 5.** Validation of free-surface elevation ($\eta$) at each WG and wave-induced velocities ($u$ and $w$) at each ADV under $W1$. Scatter plots are shown for the full 18-min simulation, with points colored according to density; the 1:1 line and relevant statistical metrics are also included.

The period-averaged non-dimensional flow-kinematics indicator $\langle p_\Omega \rangle / \langle p_0 \rangle$ is used to classify the flow into $LT$ and $HT$ zones (Fig. 2f). Using the threshold 0.8 defined in Section 4.2, the resulting $LT$ and $HT$ regions largely overlap with the pre-breaking and breaking-affected areas, respectively. This classification identifies regions where particles are expected to experience enhanced turbulent dispersion and, for non-spherical particles, increased drag variability due to turbulence-induced changes in particle orientation.

A more detailed comparison between experimental and numerical data is presented in Fig. 3, which compares the free-surface elevation ($\eta$) time series at each WG location (Fig. 1) at a sampling interval of 0.1s after excluding the first $9T$. For each location, statistical metrics including the mean ($\mu$), standard deviation ($\sigma$), $BIAS$, $Skill$, and $R^2$ are reported. Overall, the model correctly reproduces the water level variability, with $RMSE \approx 0.01$ m across all WGs, while $R^2$ ranges from 0.79 at $WG_{07}$ (beginning of the shoaling zone) to 0.93 at $WG_{09}$ (immediately before wave breaking). The main exception is $WG_{10}$, located in the swash zone within an intermittently wet–dry area, where $R^2 = 0.47$. Although this lower correlation indicates that some local fluctuations are not fully captured, the relatively high $Skill$ of 0.81 suggests that the model still reproduces the general temporal evolution of the water level at this location.

Finally, Fig. 4 shows the validation of wave-induced velocities at the ADV locations. Panels a-b compare the horizontal ($u$) and vertical ($w$) velocity time series, respectively. Consistent with the free-surface results, the model reproduces the laboratory velocity records with low errors and high correlations. Horizontal-velocity errors increase from $RMSE \approx 0.02$ m/s in the shoaling region to ≈0.08 m/s near the breaking zone, while vertical-velocity $RMSE$ values are generally smaller in shoaling regions and remain below ≈0.08 m/s near breaking. Regarding correlations, $R^2 > 0.85$ for most locations for both $u$ and $w$. The main exceptions are $ADV_{07}$ and $ADV_{08}$, where the numerical and laboratory horizontal velocities show strong correlation ($R^2 = 0.86$ and 0.73, respectively), whereas the vertical velocities exhibit lower agreement

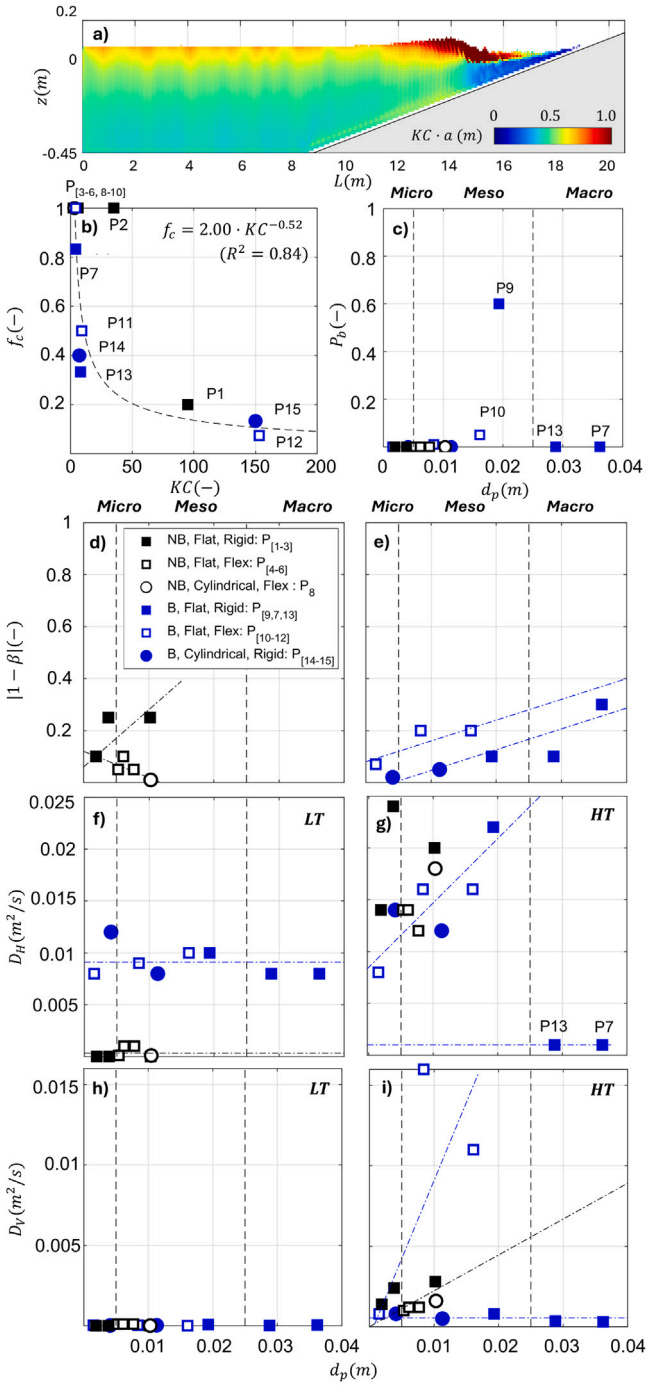


**Fig. 6.** Calibrated transport parameters under $W2$: (a) spatial distribution of $KC \cdot a$, with $KC$ the Keulegan–Carpenter number and $a$ the debris major axis; (b) oscillatory-flow correction factor $f_c$ vs $KC$; (c) beaching probability $P_b$ vs particle size $d_p$; (d–e) $|1-\beta|$ vs $d_p$ for non-buoyant and buoyant debris; (f–g) horizontal dispersion $D_H$ vs $d_p$ in $LT/HT$ regions; (h–i) vertical dispersion $D_V$ vs $d_p$ in $LT/HT$ regions. Dash-dot lines indicate emerging trends, and vertical dashed lines delineate micro-, meso-, and macro-size classes. The legend encodes buoyancy (NB/B), shape (squares = flat; circles = cylindrical), and flexibility (filled = rigid; open = flexible).

($R^2$ close to 0 and 0.43, with $Skill$ of 0.22 and 0.43, respectively). These differences can be attributed to small uncertainties in the exact vertical position of the sensors and/or to 3D flow structures generated by wave breaking in the laboratory, which cannot be fully represented by the 2DV numerical model.

In addition to $W2$, an independent validation under wave condition $W1$ is presented in Fig. 5. Laboratory and modeled free–surface elevation and wave–induced velocities are compared using scatter-density plots and summary statistics. For free-surface elevation, the model shows excellent agreement across the offshore and shoaling regions ($WG_{01}$–$WG_{07}$), with $RMSE \approx 0.01$ m and high correlations ($R^2 > 0.96$). As expected, performance decreases in the breaking, surf, and intermittently wet–dry swash zones ($WG_{08}$–$WG_{10}$), where the signal becomes strongly non–stationary and small phase shifts are amplified ($R^2 = 0.77$ at $WG_{08}$, and $R^2 = 0.50$ and 0.41 at $WG_{09}$ and $WG_{10}$, respectively). For horizontal velocities, agreement remains strong at $ADV_{01}$–$ADV_{03}$ ($RMSE \approx 0.03$–$0.05$ m/s, $R^2 > 0.95$) in the early shoaling region and at $ADV_{04}$–$ADV_{06}$ ($RMSE \approx 0.10$ m/s, $R^2 > 0.84$) in the breaking region, while it decreases near the surf–swash transition ($ADV_{07}$–$ADV_{08}$, $RMSE \approx 0.20$ m/s, $R^2 \approx 0.60$). Vertical velocities exhibit lower correlations overall ($R^2 \approx 0.45$–$0.61$), with the lowest agreement at $ADV_{07}$ ($R^2 = 0.26$), consistent with the discrepancies previously observed for $W2$.

Overall, the hydrodynamic validation for both $W2$ and $W1$ confirms that the numerical wave flume reproduces the primary free–surface and current statistics across both conditions, supporting its use as hydrodynamic forcing for the Lagrangian debris simulations. Accurately capturing the flow structure in both horizontal and vertical directions, as well as the turbulence patterns throughout the full water column, is particularly relevant for macro- and meso-inertial debris, since their transport is strongly influenced by velocity variations along both directions. The resolved velocity fields, together with the $LT$–$HT$ classification, define the hydrodynamic forcing and turbulence–dependent parameterizations driving the Lagrangian tracking model.

### 5.2. Calibration of Lagrangian transport, dispersion, and retention parameters - wave condition W2

Prior to analyzing debris transport, Lagrangian model parameters are calibrated for $W2$ by comparing simulated and laboratory time series of $C(\%)$ for the full set of 15 P$i$. Calibration was performed independently for each P$i$, exploring candidate parameter sets within the ranges reported in Table 2. For each candidate set, modeled and observed concentration time series were compared across the five cross-shore zones and both initial configurations ($IC_{SW}$ and $IC_{UD}$) using the $4T$-window evaluation protocol described in Section 4.3. The optimal parameter set was selected primarily by minimizing the aggregated $RMSE$ across zones and initial configurations, with $R^2$ considered as a secondary indicator to assess agreement in temporal trends. $MAE$ and $Skill$ are reported as complementary diagnostics. The resulting calibrated parameters and performance metrics are summarized in Table 3 and illustrated in Fig. 7.

Overall, the calibration results (Table 3) show consistently low errors across all materials, with $RMSE \approx 0.03$-$0.08$ and $MAE < 0.06$. Skill scores typically exceed 0.95, and $R^2$ ranges between 0.84 and 0.99. All correlations are statistically significant ($p \ll 0.05$). As expected, the least accurate results correspond to the largest and most flexible materials (P10 and P11), whose deformation and more complex hydrodynamic response introduce additional variability that is more difficult to capture with a single parameterization. Nevertheless, these results indicate that a single, material-specific parameter set is sufficient to reproduce with high accuracy both the transient cross-shore evolution and the final spatial distribution of P$i$.

Fig. 6 summarizes the dependence of the calibrated parameters on hydrodynamic forcing and particle properties. The spatial distribution of $KC \cdot a$ derived from the numerical wave field (panel a) is used to define a representative $KC$ for each P$i$, by accounting only for $a$. Values generally increase shoreward, reaching their maximum in the breaking region and the inner surf zone, where horizontal flow excursions are enhanced in the near-surface layers. This behavior is consistent with buoyant particles experiencing larger oscillatory displacements than

particles located deeper in the water column. The resulting $KC$ is then used in panel b to relate the correction factor $f_c$ to the oscillatory-flow forcing.

Across the range of plastic characteristics considered, $f_c$ exhibits a decreasing power-law dependence on $KC$, with $R^2 = 0.84$ (panel b). Large particles associated with small $KC$ values, where flow excursions are modest relative to debris size, show $f_c$ values close to unity, consistent with quasi-steady drag behavior. In contrast, smaller particles subjected to large oscillatory displacements (high $KC$) require $f_c \ll 1$, indicating a substantial reduction in effective drag under strongly oscillatory conditions, in which boundary-layer development, flow reversal, and vortex shedding in the particle surroundings become dominant.

Panels d-e show $|1-\beta|$, which quantifies how similar an item's motion is to that of a water particle, as a function of volume-equivalent sphere diameter $d_p$ for non-buoyant and buoyant debris, respectively. For non-buoyant, flat, and rigid debris, $|1-\beta|$ tends to increase with $d_p$, suggesting a growing deviation from passive-tracer behavior, although the limited number of points makes this trend only indicative. In contrast, flexible, elongated non-buoyant debris show the opposite behavior: larger strips exhibit smaller $|1-\beta|$, likely because greater flexibility allows them to align with the flow. Buoyant debris generally show an increasing trend of $|1-\beta|$ with size, reflecting stronger inertial effects for larger macro-debris.

The calibrated dispersion coefficients exhibit systematic differences between the regions before and after wave breaking across buoyancy classes (Fig. 6f-i). Horizontal dispersion is very small for non-buoyant debris in the $LT$ region (panel f), $D_{\mathrm{H}}^{\mathrm{LT}} \approx 10^{-5}$–$10^{-3}$ m$^2$/s, and increases substantially for buoyant debris, reaching values of the order of $10^{-2}$ m$^2$/s. In both buoyancy classes, $D_{\mathrm{H}}^{\mathrm{LT}}$ shows negligible dependence on particle size. In the $HT$ region (panel g), $D_{\mathrm{H}}^{\mathrm{HT}}$ is typically of the order of $10^{-2}$ m$^2$/s and tends to increase with particle size for both buoyant and non-buoyant debris, except for the highly buoyant mask-like materials P7 and P13. For these materials, values remain around $10^{-3}$ m$^2$/s, likely due to their very low density, which confines them near the surface and limits cross-shore dispersion relative to other buoyant debris. Vertical dispersion is systematically smaller than horizontal dispersion for all materials. The dispersion anisotropy ratio $r_D = D_{\mathrm{V}}/D_{\mathrm{H}}$ remains $\leq 1$ for all calibrated cases. In $LT$ conditions, $r_D$ spans $5\times10^{-4}$ to 1 with a median of $7\times10^{-3}$, whereas in $HT$ conditions it shifts to higher values, spanning $4\times10^{-2}$ to 1 with a median of $10^{-1}$. In $LT$ conditions (panel h), $D_{\mathrm{V}}^{\mathrm{LT}}$ falls in the range $10^{-6}$–$10^{-4}$ m$^2$/s. In $HT$ (panel i), most debris is concentrated around $D_{\mathrm{V}}^{\mathrm{HT}} \approx 10^{-3}$ m$^2$/s, whereas the larger and more flexible buoyant debris reach values of the order of $10^{-2}$ m$^2$/s, approaching their corresponding horizontal dispersion magnitudes.

Finally, retention in the swash zone is captured through the calibrated beaching probability $P_b$ (panel c). For most materials, $P_b$ is zero, indicating frequent mobilization and re-mobilization by waves and swash dynamics. A notable exception is macroplastic P9, a flat, relatively rigid A4-sized sheet, whose behavior is best reproduced with $P_b = 0.6$, suggesting a strong tendency to be trapped within the swash zone. In contrast, similarly sized but more flexible P10 exhibits a much lower $P_b$ of approximately 0.05, as its deformability under wave and swash forcing likely reduces the effective area exposed to the flow and prevents the stable bed contact required for beaching. Mask-like materials (P7 and P13) also exhibit negligible $P_b$, likely due to their fibrous structure and high buoyancy, which promote re-suspension rather than persistent beaching.

To further evaluate the robustness of the calibrated parameter sets, additional sensitivity analyses address stochastic variability and temporal discretization. Due to the stochastic formulation, individual particle trajectories may differ between realizations initialized with different random seeds. However, since the focus of this study is on group-scale behavior rather than individual trajectories, variations in $\mathbf{D}$ or $P_b$ produce only minor fluctuations in particle concentrations and are not expected to alter the overall cross-shore distribution patterns. Across repeated realizations of representative cases, differences in $C(t)$ remained small ($\Delta C \leq 0.1$ percentage points, pp) and aggregated $RMSE$ showed negligible variation ($\Delta RMSE \leq 0.03\%$), confirming the stability of the calibrated solutions at the ensemble scale.

Sensitivity to the integration time step is also examined. Simulations with $\Delta t = 0.05$, 0.1, and 0.2 s show that the adopted value $\Delta t = 0.1$ s provides stable concentration evolutions. Differences relative to $\Delta t = 0.05$ s are minor ($\Delta C = 0.06$–$0.15$ pp), whereas slightly larger deviations are observed for $\Delta t = 0.2$ s ($\Delta C = 0.07$–$0.24$ pp). Corresponding $RMSE$ differences remain small ($\leq 0.06\%$), supporting the numerical robustness of the calibrated configuration.

### 5.3. Validation of Lagrangian transport, dispersion, and retention parameters - wave condition W1

In addition to the calibration performed for wave condition $W2$ (Section 5.2), the Lagrangian transport, dispersion, and retention parameters are validated under $W1$ using the same parameter sets. The coefficient $f_c$ is estimated according to the expression shown in Fig. 6b.

Overall, the model successfully reproduces the transport and accumulation patterns observed in the laboratory for $W1$ (blue lines versus black-edged markers in Fig. 12). Statistical metrics reported in Table 4 indicate good agreement: for non-buoyant materials, $RMSE$ is generally around or below 0.10%, while slightly higher values are observed for buoyant debris. Correlations are high, with $R^2 > 0.70$ and $Skill > 0.90$ for most materials. These results confirm that the calibrated parameter sets maintain consistent predictive capability under a different wave condition. The main discrepancies are associated with buoyant materials P9, P10, P11, and P12.

For the flat macroplastics P9 and P10, which in $W2$ were better represented with $P_b > 0$ (likely due to their large bottom contact area required for beaching), the results under $W1$ and $IC_{\mathrm{SW}}$ improve significantly when $P_b = 0$. Under this more energetic condition, stronger removal forces reduce the likelihood of beaching, and the configuration with $P_b = 0$ provides a closer match to the experimental data. The adjusted results (Fig. 12, green line) show a reduction in $RMSE$ by more than half and achieve $R^2 > 0.70$.

For the flexible materials P11 and P12 under $IC_{\mathrm{UD}}$, the model predicts greater accumulation in the surf zone rather than in the swash zone, as observed experimentally. Shifting the surf–swash boundary from 16.7 m to 16.2 m reduces the $RMSE$ by 0.03–0.07% and increases $R^2$ to above 0.77, indicating that the discrepancy is primarily due to a small spatial offset rather than a fundamental mismatch in transport dynamics.

Additionally, for the larger rigid buoyant elements (P7, P13, and P14), the calibrated parameter set reproduces the overall transport trends, with $RMSE \approx 0.10\%$ and $R^2 > 0.86$, although the simulated onshore transport is faster and more intense than observed experimentally. A slight reduction in the $\beta$ parameter improves the agreement, yielding $RMSE \approx 0.05\%$ and $R^2 > 0.90$. This improvement can be explained since reducing the added-mass effect and therefore particle inertia, allows the particles to respond more consistently to the drag-corrected hydrodynamic forcing, mitigating the overestimation of onshore transport. The sensitivity of the results to $\beta$ highlights the importance of testing parameter sets under a broader range of hydrodynamic conditions to ensure robust calibration.

In summary, the validation under $W1$ indicates that the parameter sets calibrated for $W2$ maintain consistent predictive capability under a different laboratory wave condition. Some material-specific sensitivities are observed, particularly for buoyant elements; however, the overall transport dynamics are well reproduced within the tested experimental range, demonstrating the reliability of the calibrated parameters.

**Table 3**
Calibrated parameters of the Lagrangian tracking model under $W2$ and corresponding average statistical performance metrics, computed from the temporal evolution of particle concentrations in the five cross-shore zones for both initial conditions ($IC_{SW}$ and $IC_{UD}$). All simulations were performed with $N = 1000$ particles.

| P$i$ | $f_c$/KC (−)/(−) | $\beta$ (−) | $D_H^{LT}$ ($m^2/s$) | $D_H^{HT}$ ($m^2/s$) | $D_V^{LT}$ ($m^2/s$) | $D_V^{HT}$ ($m^2/s$) | $P_b$ (−) | RMSE (%) | MAE (%) | Skill (−) | $R^2$ (−) | p-value (−) |
|---|---|---|---|---|---|---|---|---|---|---|---|---|
| P1 | 0.20/92 | 0.90 | 1.00E−05 | 1.40E−02 | 1.00E−06 | 1.40E−03 | 0 | 0.028 | 0.019 | 0.996 | 0.985 | 0.000 |
| P2 | 1.00/33 | 0.75 | 1.00E−05 | 2.40E−02 | 1.00E−06 | 2.40E−03 | 0 | 0.032 | 0.022 | 0.994 | 0.980 | 0.000 |
| P3 | 1.00/6 | 0.75 | 1.00E−05 | 2.00E−02 | 1.00E−05 | 2.80E−03 | 0 | 0.033 | 0.021 | 0.994 | 0.978 | 0.000 |
| P4 | 1.00/4 | 0.95 | 1.00E−04 | 1.40E−02 | 1.00E−04 | 1.00E−03 | 0 | 0.047 | 0.035 | 0.985 | 0.945 | 0.000 |
| P5 | 1.00/3 | 0.90 | 1.00E−03 | 1.4E−02 | 1.00E−04 | 1.20E−03 | 0 | 0.045 | 0.032 | 0.990 | 0.962 | 0.000 |
| P6 | 1.00/1 | 0.95 | 1.00E−03 | 1.20E−02 | 1.00E−04 | 1.20E−03 | 0 | 0.058 | 0.039 | 0.985 | 0.945 | 0.000 |
| P8 | 1.00/3 | 0.99 | 1.00E−04 | 1.80E−02 | 1.00E−05 | 1.60E−03 | 0 | 0.029 | 0.021 | 0.995 | 0.986 | 0.000 |
| P9 | 1.00/4 | 1.10 | 1.00E−02 | 2.20E−02 | 7.00E−05 | 8.00E−04 | 0.6 | 0.046 | 0.029 | 0.989 | 0.962 | 0.000 |
| P10 | 1.00/4 | 1.20 | 1.00E−02 | 1.60E−02 | 5.00E−06 | 1.10E−02 | 0.05 | 0.077 | 0.055 | 0.955 | 0.883 | 0.000 |
| P11 | 0.50/9 | 1.20 | 0.90E−02 | 1.60E−02 | 4.00E−05 | 1.60E−02 | 0.01 | 0.078 | 0.059 | 0.962 | 0.863 | 0.000 |
| P12 | 0.07/153 | 1.07 | 0.80E−02 | 0.80E−02 | 4.00E−05 | 8.00E−04 | 0 | 0.037 | 0.031 | 0.986 | 0.963 | 0.000 |
| P14 | 0.40/7 | 1.05 | 0.80E−02 | 1.20E−02 | 3.00E−05 | 5.00E−04 | 0 | 0.067 | 0.038 | 0.955 | 0.842 | 0.000 |
| P15 | 0.13/150 | 1.02 | 1.20E−02 | 1.40E−02 | 2.00E−05 | 8.00E−04 | 0 | 0.036 | 0.028 | 0.980 | 0.954 | 0.000 |
| P7 | 0.83/4 | 1.30 | 0.80E−02 | 1.00E−03 | 5.00E−05 | 3.00E−04 | 0 | 0.048 | 0.030 | 0.980 | 0.924 | 0.000 |
| P13 | 0.33/8 | 1.10 | 0.80E−02 | 1.00E−03 | 2.00E−05 | 3.50E−04 | 0 | 0.039 | 0.027 | 0.989 | 0.958 | 0.000 |

**Table 4**
Validation of the Lagrangian tracking model under $W1$, with adjusted parameters and corresponding statistical metrics for both calibrated (C) and adjusted values (A).

| P$i$ | Parameter | C/A | RMSE (%) C/A | MAE (%) C/A | Skill (-) C/A | $R^2$ (-) C/A | p-value (-) C/A |
|---|---|---|---|---|---|---|---|
| P1 | – | – | 0.057/- | 0.040/- | 0.983/- | 0.938/- | 0.000/- |
| P2 | – | – | 0.086/- | 0.057/- | 0.963/- | 0.874/- | 0.000/- |
| P3 | – | – | 0.039/- | 0.024/- | 0.994/- | 0.979/- | 0.000/- |
| P4 | – | – | 0.093/- | 0.061/- | 0.958/- | 0.874/- | 0.000/- |
| P5 | – | – | 0.134/- | 0.091/- | 0.920/- | 0.757/- | 0.000/- |
| P6 | – | – | 0.093/- | 0.066/- | 0.958/- | 0.859/- | 0.000/- |
| P8 | – | – | 0.094/- | 0.066/- | 0.958/- | 0.853/- | 0.000/- |
| P9 | $P_b$ (-) | 0.60/0 | 0.147/0.068 | 0.099/0.049 | 0.888/0.946 | 0.676/0.823 | 0.000/0.000 |
| P10 | $P_b$ (-) | 0.05/0 | 0.260/0.099 | 0.198/0.072 | 0.586/0.892 | 0.352/0.704 | 0.000/0.000 |
| P11 | L. Surf-Swash (m) | 16.7/16.2 | 0.102/0.070 | 0.074/0.051 | 0.827/0.945 | 0.617/0.821 | 0.000/0.000 |
| P12 | L. Surf-Swash (m) | 16.7/16.2 | 0.166/0.109 | 0.118/0.081 | 0.694/0.906 | 0.456/0.771 | 0.000/0.000 |
| P14 | $\beta$ (-) | 1.05/1.02 | 0.160/0.063 | 0.108/0.042 | 0.919/0.972 | 0.856/0.914 | 0.000/0.000 |
| P15 | – | – | 0.084/- | 0.061/- | 0.945/- | 0.815/- | 0.000/- |
| P7 | $\beta$ (-) | 1.30/1.10 | 0.106/0.054 | 0.067/0.034 | 0.976/0.992 | 0.946/0.970 | 0.000/0.000 |
| P13 | $\beta$ (-) | 1.10/1.05 | 0.126/0.056 | 0.086/0.040 | 0.956/0.985 | 0.906/0.958 | 0.000/0.000 |

### 5.4. Cross-shore transport and accumulation patterns

Using the calibrated and validated parameters in Sections 5.2 and 5.3, the Lagrangian results are analyzed in terms of cross-shore transport and accumulation patterns for each P$i$. Fig. 7 presents the concentration metric, $C(t)$, under wave condition $W2$, while Fig. 12 shows the corresponding results for $W1$. In both cases, $C(t)$ is evaluated across the five cross-shore zones (offshore, shoaling, breaking, surf, and swash) for all 15 P$i$ and for both initial conditions ($IC_{SW}$ and $IC_{UD}$).

Across both wave conditions, for non-buoyant materials, under $IC_{SW}$ (panel a in both figures), the model reproduces the early export from the swash zone and the subsequent accumulation near the breaking region, in agreement with laboratory observations. Under $IC_{UD}$ (panel b in both figures), a substantial fraction of the material remains offshore, while concentrations in the shoaling zone decrease as particles are advected toward the breaking region, where they accumulate. This preferential accumulation is consistent with the resolved circulation pattern, characterized by a near-bed offshore-directed return flow (undertow) and a flow-separation (undertow detachment) zone in the vicinity of the breaking point.

Buoyant materials show more pronounced differences among debris types. Under $IC_{SW}$ (panel c in both figures), the simulations capture progressive offshore transport and dispersion. Resulting concentrations depend on the characteristics of each P$i$, which determine the flow layer with which the particles interact and, consequently, their net transport direction. Macro- and meso-sized sheets (P9, P10, P11) tend to redistribute toward the surf, breaking, and even shoaling areas, likely because their size and partial submergence increase interaction with sub-surface currents. In contrast, microsheets (P12), cylindrical straw-like debris (P14 and P15), and highly buoyant mask-like materials (P7 and P13) accumulate preferentially in the surf and swash regions. The cylindrical shape of the straws, the small size of P12, and the high buoyancy of mask-like materials may all promote alignment with near-surface flow, favoring accumulation closer to the shore. Similarly, under $IC_{UD}$ (panel d in both figures), the transport and preferred accumulation region of each buoyant item follow the same patterns, with macro- and meso-sized sheets redistributing toward the shoaling and breaking zones, while microsheets, straw-like debris, and mask-like materials accumulate in the surf and swash regions. Across all wave conditions, initial releases, and all materials, the numerical results generally follow the laboratory data with minimal deviations, capturing the timing of transitions between zones and confirming the overall quality of the calibration, consistent with the performance metrics reported in Table 3.

To complement the quantitative assessment, a frame-based comparison focused on $W2$ is performed to verify whether the model reproduces the debris pathways and spatial distribution observed in the laboratory. Figs. 8, 9, 10, and 11 compare experimental frames with simulated particle clouds for two representative microplastics: non-buoyant P1 (red markers) and buoyant P12 (blue markers), under both initial-release configurations, at $t$ = 0, 10, 40, 500, and 1080 s.

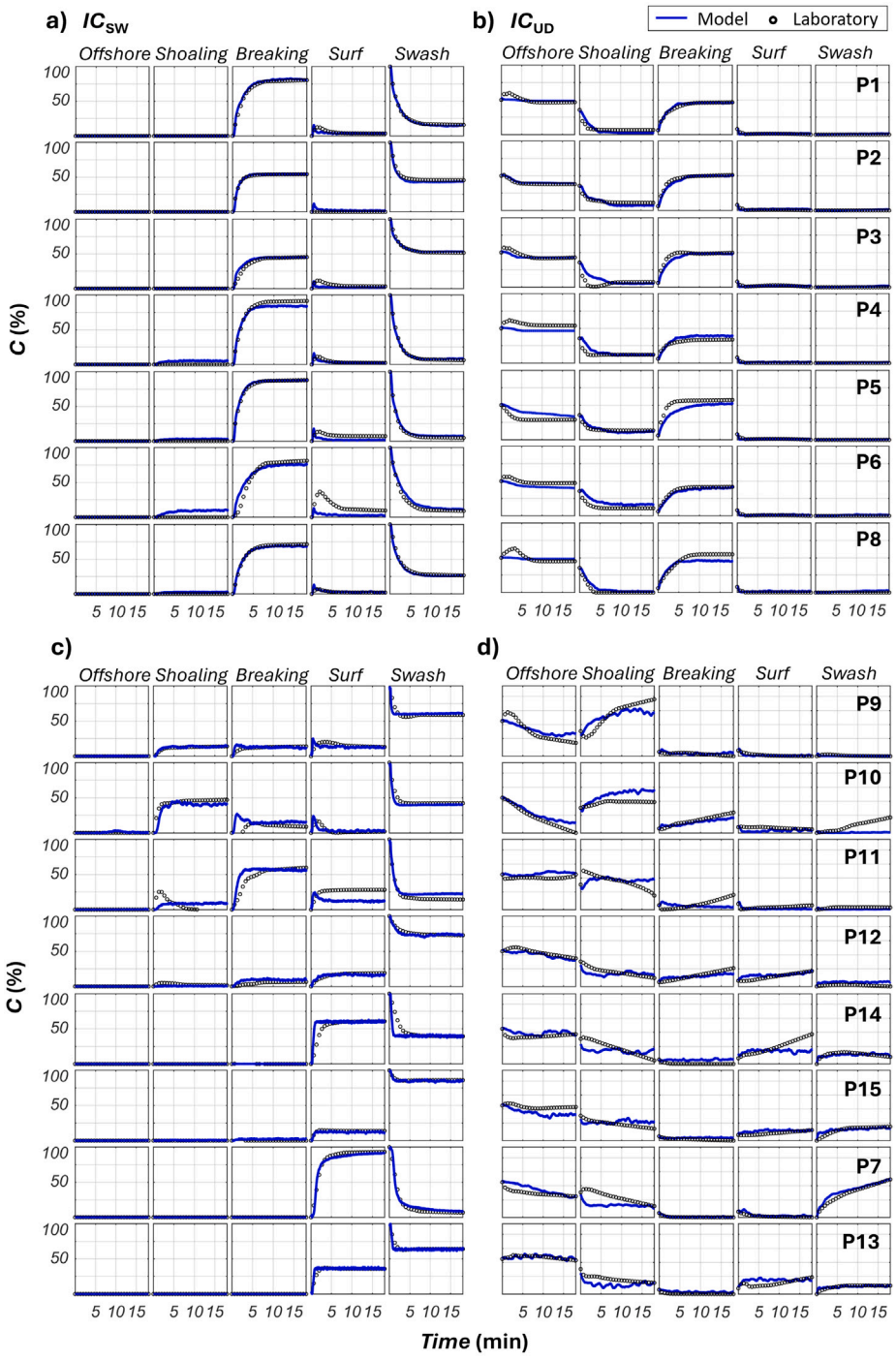


**Fig. 7.** Calibration results ($W2$): temporal evolution of concentrations $C(\%)$ of P$i$ across the offshore, shoaling, breaking, surf, and swash zones for non-buoyant (upper panels a–b) and buoyant (lower panels c–d) debris. Left panels a/c correspond to $IC_{SW}$, while right panels b/d correspond to $IC_{UD}$.

The simulations reproduce the key spatial patterns observed in the laboratory: P1 converges toward the breaking region under both initial conditions, while P12 is predominantly transported toward the swash zone. Furthermore, persistent offshore deposits are observed for both materials under $IC_{UD}$. Overall, the simulated clouds closely match the experiments in terms of spatial extent, particle clustering, and temporal evolution, confirming that the calibrated model accurately reproduces both integrated concentration trends and realistic transport pathways.

As for the full set of P$i$, Fig. 13 summarizes the model's ability to reproduce the final cross-shore distributions of plastic debris across all regions. Each marker compares the final concentration in a given zone from the numerical simulations ($FC_{num}$) with the corresponding laboratory measurements ($FC_{lab}$). For $IC_{SW}$ (left panel), most points lie close to the 1:1 line ($R^2 = 0.98$), indicating that the model captures both the strong final trapping of buoyant materials in the swash and surf zones and the near-complete removal of non-buoyant types from these areas to the breaking point. For $IC_{UD}$ (right panel), the scatter is slightly larger but still shows a clear linear correlation ($R^2 = 0.85$). Overall, these results confirm that the calibrated parameter set reproduces both the temporal dynamics and the net cross-shore redistribution of plastic materials after prolonged wave forcing.

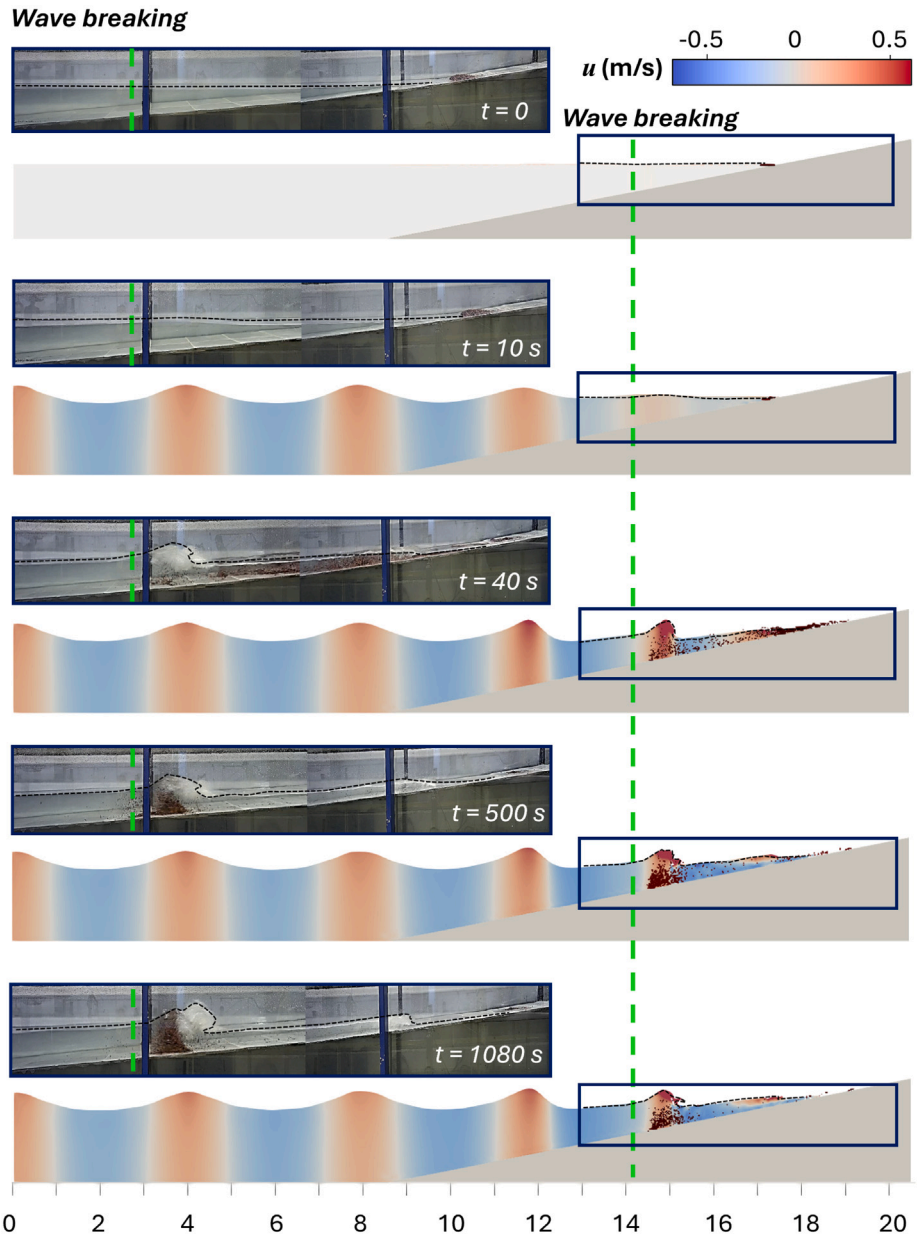


**Fig. 8.** Qualitative comparison of experimental and numerical plastic-debris positions at selected times ($t$) for the non-buoyant material P1 (red markers) with initial condition $IC_{SW}$ under $W2$.

## 6. Discussion

### 6.1. Debris-typology-dependent transport, accumulation, and retention

This study, supported by a laboratory-validated numerical framework, demonstrates that surf-zone transport, dispersion, and accumulation of plastic debris are governed by the combined effects of wave-breaking hydrodynamics and debris typology (buoyancy, size, shape, and flexibility). Under these conditions, tracer-like assumptions may be inaccurate because typology controls (i) the effective depth over which the flow is sampled and (ii) the degree to which debris deviates from passive drift. These deviations arise from particle–flow decoupling, wave-induced oscillatory motion, turbulence-driven exchange, and swash-zone beaching, leading to divergent transport pathways and accumulation hotspots under identical wave forcing.

A primary control on transport mechanisms is the vertical position of debris within the water column. Buoyancy, together with size and shape, determines which flow layers are sampled and, consequently, which components of the nearshore circulation dominate transport. Non-buoyant, flat debris preferentially interacts with deeper layers, where mean circulation and breaking-induced detachment promote convergence toward the surf zone. Highly buoyant, surface-oriented items remain in the upper layer, where onshore advection and swash-zone interactions enhance retention. Partially submerged debris typically samples multiple layers, exhibiting intermediate behaviors that cannot be captured by purely surface- or near-bed drift assumptions, nor by depth-averaged representations (Fig. 2c).

Deviations from passive drift can be interpreted through the concept of “effective inertia”. The added-mass contribution reflects the acceleration of the surrounding water moving with the debris and depends on submerged volume, geometry, and, for flexible items, evolving shape. For rigid debris, added mass is typically enhanced, leading to more pronounced deviations from passive motion, whereas flexibility can reduce this contribution by promoting deformation and streamwise alignment. For buoyant debris, however, the opposite effect may occur:

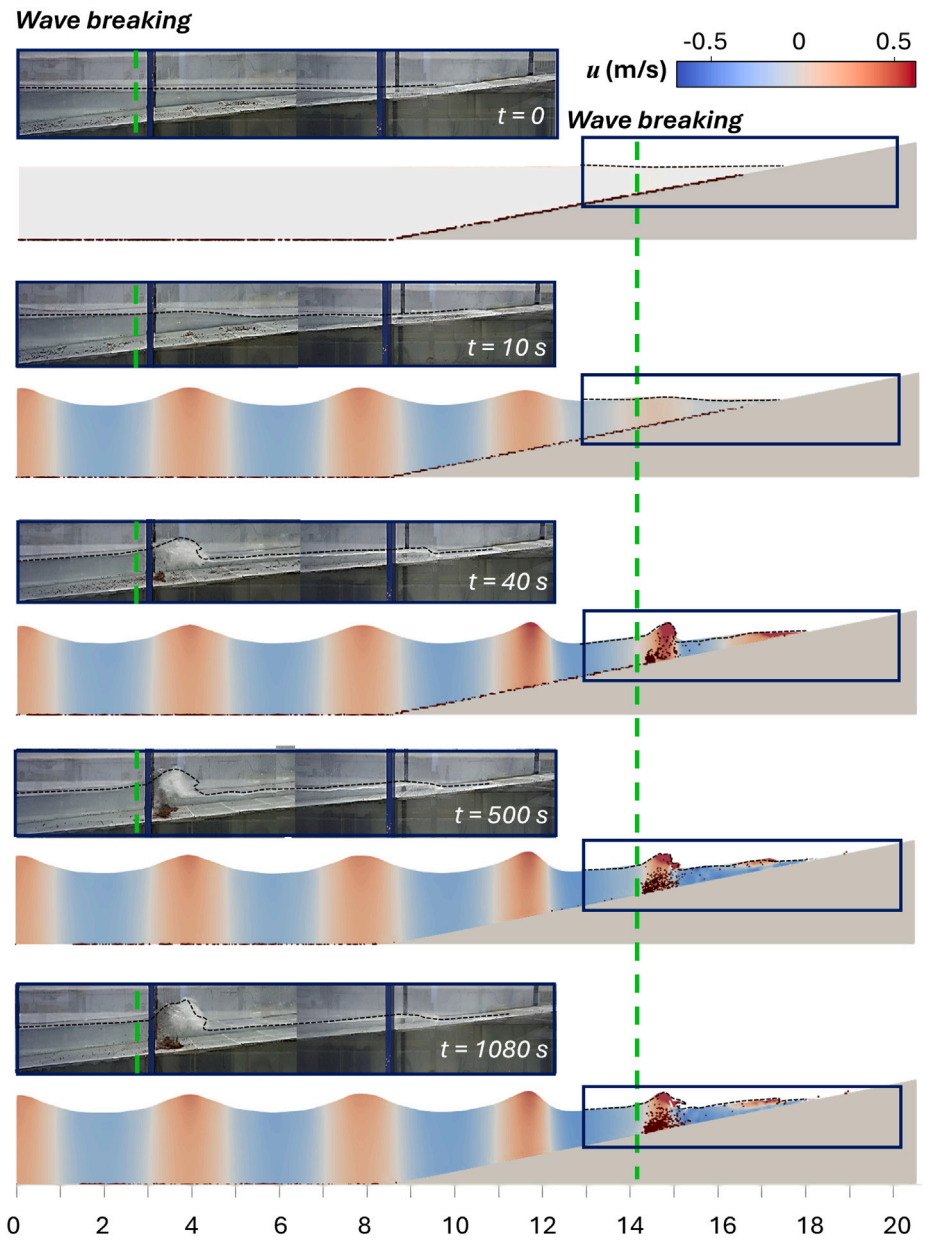


**Fig. 9.** Qualitative comparison of experimental and numerical plastic-debris positions at selected times ($t$) for the non-buoyant material P1 (red markers) with initial condition $IC_{\mathrm{UD}}$ under $W2$.

flexibility can increase mean submergence, thereby enhancing added-mass effects. In this sense, buoyancy modulates added mass primarily through immersion (Fig. 6d–e).

Oscillatory wave forcing can further contribute by modifying the effective drag in a typology-dependent manner. Relative motion between debris and water depends on the particle's ability to reorient and accelerate, as well as on the local unsteadiness of the flow (wave period and acceleration). When the wave-orbital excursion over a cycle is large relative to a characteristic debris length, each particle reorients differently depending on its size, shape, flexibility, and submergence, altering effective drag and, consequently, its contribution to effective inertia. Buoyancy further modulates these effects by controlling submergence and, hence, the depth-dependent intensity of oscillatory wave kinematics (Fig. 6a–b).

Turbulence and swash-zone interactions shape debris dispersion and retention. Post-breaking turbulence enhances cross-shore dispersion, particularly for debris sampling multiple layers, and promotes vertical exchange (Fig. 6g, i). Swash-zone retention depends on both particle-flow and particle-bottom interactions. Non-buoyant debris shows negligible retention due to sustained submergence, favoring rapid offshore transport. Small buoyant particles near the surface can persist through hydrodynamic trapping alone, consistent with Rahmani and Stocchino (2026), while larger buoyant debris is more easily released as intermittent sampling of deeper layers exposes them to offshore currents. However, for these larger items, retention also depends on particle-bottom interactions: rigid macrodebris is more prone to become trapped in swash zones than flexible debris of similar size, likely due to reduced flow alignment and higher friction from larger contact areas. Together, these mechanisms define accumulation hotspots in the surf and swash zones (Fig. 6c).

### 6.2. Surf-zone hydrodynamics and particle-scale mechanisms

OpenFOAM® (Section 2.1) with the RSM-$\omega$ turbulence closure (Li et al., 2022) resolves wave-breaking undertow, vertical shear, and

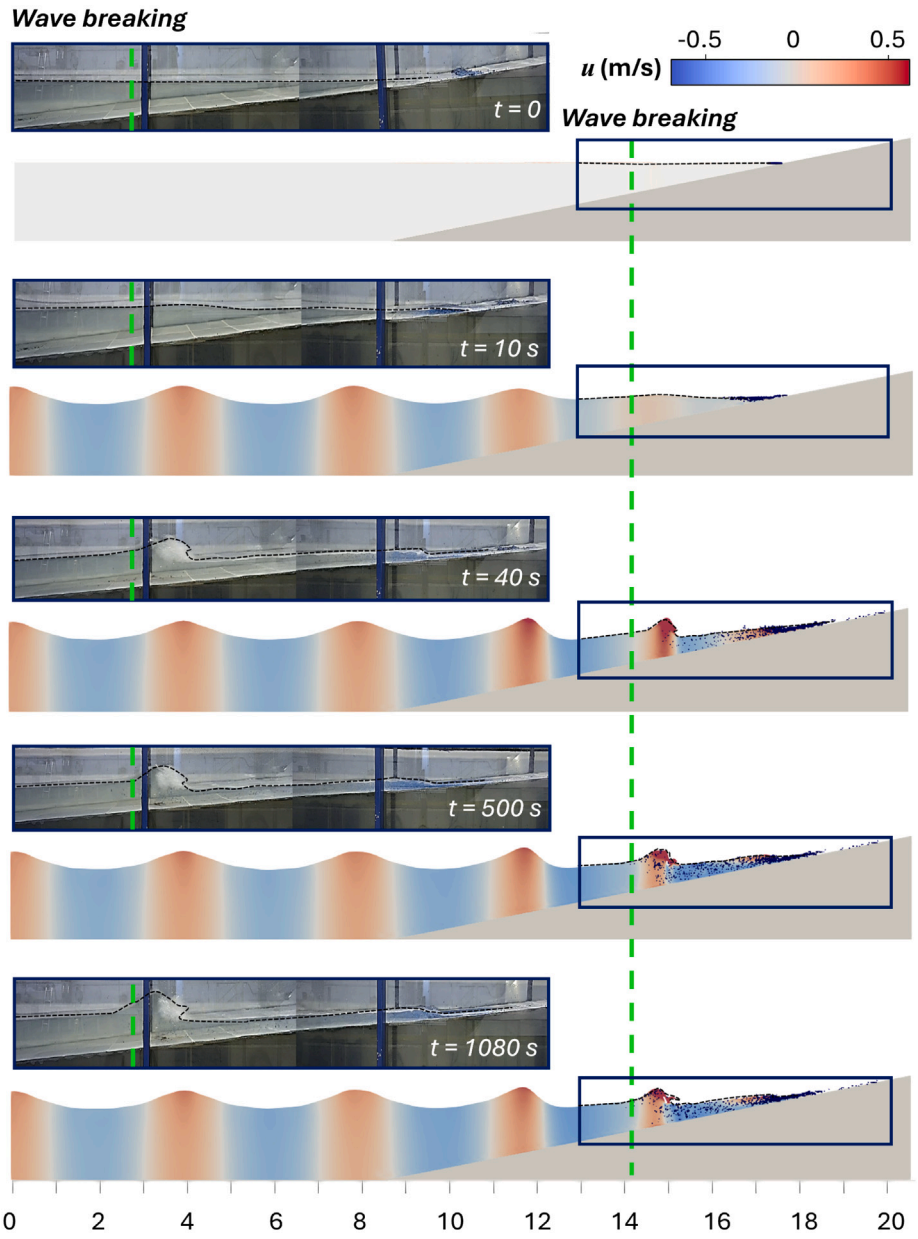


**Fig. 10.** Qualitative comparison of experimental and numerical plastic-debris positions at selected times ($t$) for the buoyant material P12 (blue markers) with initial condition $IC_{SW}$ under $W2$.

turbulence gradients generated by spilling breaking waves. These processes drive vertical mixing and modulate debris transport, dispersion, and retention in a typology-dependent manner. Validation against laboratory measurements confirms the suitability of the simulated fields for interpreting debris transport: water levels exhibited $RMSE \approx 0.01$ m with $R^2 > 0.79$ in the pre-breaking and breaking regions, and horizontal velocities $RMSE \approx 0.02$-$0.10$ m/s with $R^2 > 0.84$ in the same regions.

The Lagrangian module (Section 2.2) extends inertial formulations from previous studies (e.g., De Leo and Stocchino, 2022; Stocchino et al., 2019; Rahmani and Stocchino, 2026) to finite-size, non-spherical particles across a range of turbulent intensities. Particle–flow interactions account for drag, buoyancy, and added mass, complemented by a subgrid stochastic representation of unresolved dispersion and a probabilistic beaching scheme. An effective-velocity approach provides a first-order approximation of translational effects, similar to Faxén-type corrections, by sampling the local flow at representative points on the particle surface (Section 2.2.2). Orientation-dependent drag coefficients capture anisotropic particle behavior (DiBenedetto et al., 2018; Nayak et al., 2018), while an oscillatory-flow correction is applied through a $KC$–dependent factor ($R^2 = 0.84$; Fig. 6b). The particle-specific $\beta$ coefficient, independent of orientation, quantifies added-mass contributions, varying with particle size, shape, buoyancy, and flexibility (Fig. 6d–e).

Subgrid-scale particle dispersion is represented using a stochastic (Brownian) formulation (e.g., Reeks, 1988; Drossinos and Reeks, 2005; Boi, 2019; De Leo and Stocchino, 2022), implemented as a calibrated, anisotropic, piecewise-constant scheme distinguishing two transport regimes: low pre-breaking turbulence ($LT$) and high post-breaking turbulence ($HT$). Beaching is treated probabilistically (Lebreton et al., 2012; Critchell et al., 2015; Carlson et al., 2017; Cardoso and Caldeira, 2021), and notably, even without explicit particle–bottom interactions, the model reproduces the persistence of highly buoyant, surface-trapped debris in the swash zone, consistent with laboratory observations of onshore wave-driven transport. Together, these

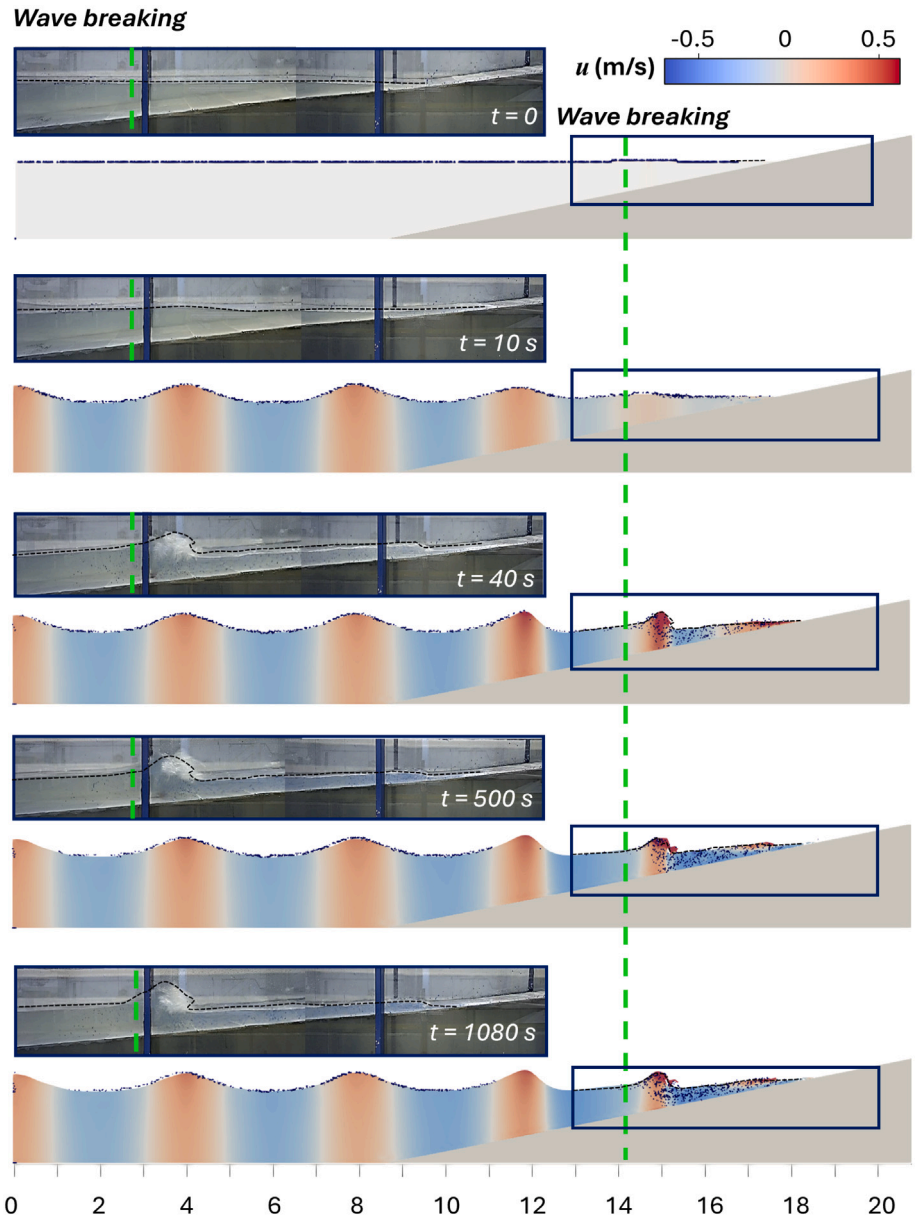


**Fig. 11.** Qualitative comparison of experimental and numerical plastic-debris positions at selected times ($t$) for the buoyant material P12 (blue markers) with initial condition $IC_{\mathrm{UD}}$ under $W2$.

mechanisms capture the main patterns of debris transport and accumulation while remaining computationally efficient and acknowledging several simplifications discussed in Section 6.4. The model achieves $RMSE \approx 0.03$-$0.10\%$ and $R^2 \approx 0.70$–$0.99$, with slightly larger deviations for specific buoyant elements (Tables 3 and 4).

### 6.3. One-way CFD–Lagrangian coupling: efficiency and applicability

One-way coupling is computationally efficient and widely used in particle-laden flows (e.g., Berrouk et al., 2007; Dehbi, 2008; Tang et al., 2015), though its application to surf-zone plastic debris remains limited (Jalón-Rojas et al., 2025; Rahmani and Stocchino, 2026). In the present framework, high-fidelity, wave-resolving CFD is coupled with an inertial Lagrangian solver to simulate finite-size, non-spherical debris from micro- to macroplastics over a laboratory surf-zone bathymetry (Section 2.3). Boundary operators for bottom and free-surface reflection, offshore removal, and probabilistic beaching are included at negligible computational cost, enabling efficient simulation of nearshore retention and shoreline interactions. Calibration and validation against laboratory experiments confirm the method's effectiveness.

The modular design allows the hydrodynamic core to be replaced depending on spatial and temporal scales of interest. While high-resolution CFD is suited for short- to medium-term, fine-scale analyses where turbulence detail is critical, phase-resolving or wave-averaged models can be used for larger domains or longer simulations, trading some turbulence detail for coverage while retaining consistent Lagrangian particle physics. At the most computationally efficient end of this hierarchy, depth-integrated models can also be coupled to the Lagrangian module by averaging the flow over depth. However, their limited representation of vertical structure and turbulence-induced mixing (relevant for simulating inertial macro- and meso-debris) typically requires additional parameterizations, adding uncertainty to the Lagrangian forcing. Overall, this modular approach enhances the ability to perform ensemble or probabilistic simulations of pollution scenarios, supporting decision-making and operational planning in coastal management.

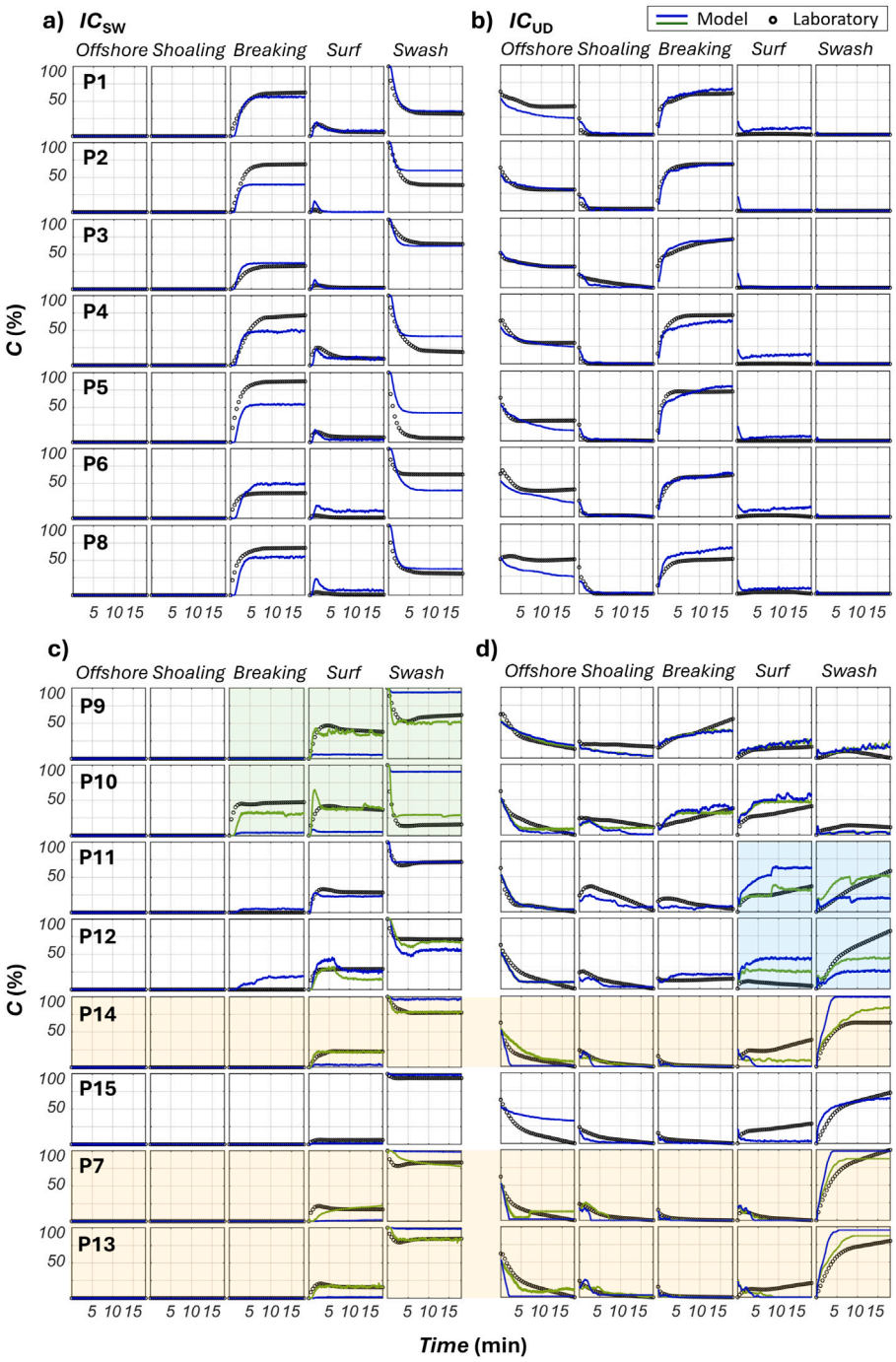


**Fig. 12.** Validation results ($W1$): temporal evolution of concentrations $C(\%)$ of P$i$ across the offshore, shoaling, breaking, surf, and swash zones for non-buoyant (upper panels a-b) and buoyant (lower panels c-d) debris. Left panels a/c correspond to $IC_{SW}$, while right panels b/d correspond to $IC_{UD}$. The blue line represents the model results with the calibrated parameter sets, and the green line shows the adjusted results after modifying $P_b$ (for P9 and P10), the surf-swash boundary ($L_{Surf-Swash}$, for P11 and P12), and $\beta$ (for P7, P13, and P14).

### 6.4. Scope, limitations and future perspectives

The calibration and validation strategy adopted in this study is conducted under regular-wave conditions of the benchmark. Model parameters are first calibrated using the $W2$ wave condition and subsequently validated against the $W1$. This choice provides controlled hydrodynamic settings in which the dominant physical mechanisms governing particle transport, dispersion, and beaching can be isolated and analyzed without the additional complexity introduced by irregular wave forcing. Within this regular-wave framework, calibration and validation are conducted across two distinct initial release configurations and a broad set of 15 debris types, allowing the robustness of the proposed formulation to be assessed under contrasted initial conditions and particle properties. Accordingly, the findings should not be interpreted as a comprehensive validation across all surf-zone conditions, but rather as a process-oriented assessment demonstrating the internal consistency and physical plausibility of the proposed CFD-Lagrangian framework under representative, well-characterized scenarios. The extension of the validation to irregular wave conditions and fully three-dimensional configurations is left for future work.

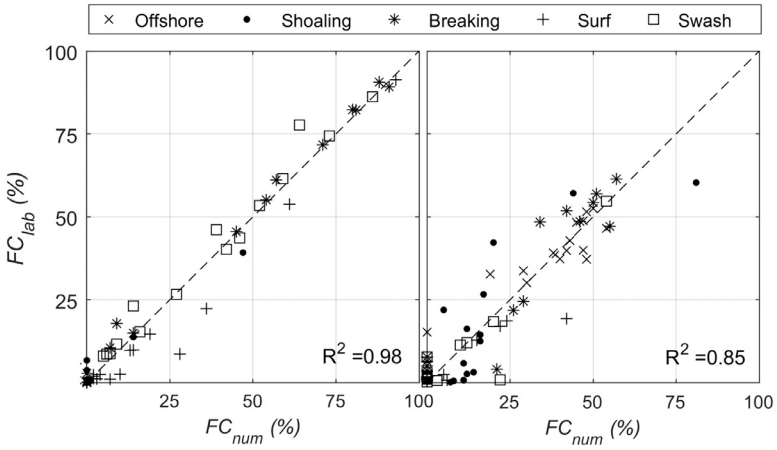


**Fig. 13.** Scatter plots comparing final concentrations of P$i$ from numerical results, $FC_{\mathrm{num}}(\%)$, and laboratory data, $FC_{\mathrm{lab}}(\%)$, for $IC_{\mathrm{SW}}$ (left panel) and $IC_{\mathrm{UD}}$ (right panel).

Within this deliberately constrained framework, certain limitations should be acknowledged. A first limitation is the computational cost of CFD simulations for reproducing wave breaking in realistic coastal settings, which would require fully three-dimensional configurations. This limitation can be partially mitigated by the framework's modular structure, allowing the use of alternative or reduced-complexity hydrodynamic solvers (Section 6.3).

At the particle scale, several higher-order effects are omitted to maintain computational efficiency, including explicit Faxén corrections, lift, unsteady history effects (Boi, 2019), and full six-degree-of-freedom (6-DOF) rigid-body rotation (Kolahdouz et al., 2021). To partially account for these omissions, leading-order finite-size and shape effects are retained through orientation-dependent parametrizations (e.g., drag coefficients and an effective-velocity sampling strategy). Particle–particle interactions (aggregation, collision-induced dispersion, hindered settling or flotation, wake sheltering, and capacity-limited trapping) are also neglected, making the approach most suitable for low- to moderate-concentration scenarios. Air-water interactions and windage are not represented, which may reduce accuracy for highly buoyant or partially emergent debris. Particle properties are assumed static, neglecting the dynamic influence of biofouling (Núñez et al., 2023a). Future work should quantify the impact of these simplifications, particularly for complex debris typologies and more energetic breaking-wave conditions.

A further topic for discussion is the simplified representation of turbulence-driven dispersion. The pragmatic assumption of piecewise-constant effective dispersions based on an $LT/HT$ classification (with $LT/HT$ defined using the non-dimensional, period-averaged flow-kinematics indicator $\langle p_\Omega \rangle / \langle p_0 \rangle$; Larsen and Fuhrman, 2018) captures unresolved mixing at low computational cost but may not fully represent the intermittent, anisotropic, and spatially heterogeneous turbulence characteristic of surf and swash zones, nor event-driven mixing associated with breaking-induced structures and bore-swash interactions (Rahmani and Stocchino, 2026). Accordingly, results should be interpreted as a first-order description of unresolved dispersion under the considered conditions. Further research is needed to develop more local and state-dependent dispersion closures (e.g., formulated as smooth functions of $\langle p_\Omega \rangle / \langle p_0 \rangle$ or related breaking indicators) and to evaluate the sensitivity of predicted concentrations and beaching patterns to these assumptions.

Related to this, dispersion anisotropy is represented through two calibrated components, $D_{\mathrm{H}}$ and $D_{\mathrm{V}}$. These coefficients act as effective Lagrangian dispersion parameters, capturing the net effect of unresolved fluctuations on the displacements of finite-size particles, and thus depend not only on the flow field but also on debris-specific dynamics (e.g., buoyancy-driven vertical layer sampling, finite-size inertia, and shape- or flexibility-dependent orientation and drag). While turbulence theory indicates that horizontal and vertical mixing are constrained by the anisotropic structure of the flow, no universally established functional relationship linking $D_{\mathrm{H}}$ and $D_{\mathrm{V}}$ exists for non-passive particles spanning a wide range of sizes, shapes, and flexibilities. In this framework, anisotropic dispersion is represented by calibrating the horizontal and vertical components, subject to the physically consistent constraint $D_{\mathrm{V}} \leq D_{\mathrm{H}}$. The calibrated parameters satisfy this constraint across all cases, with the anisotropy ratio $r_D = D_{\mathrm{V}}/D_{\mathrm{H}} \leq 1$ and typical values increasing from $\mathcal{O}(10^{-3})$ in $LT$ to $\mathcal{O}(10^{-1})$ in $HT$; moreover, values remain well below the isotropic limit in nearly all cases, approaching $r_D \approx 1$ only under $HT$ conditions for large buoyant debris, consistent with the expected structure of surf-zone turbulence.

Another limitation concerns the absorbing beaching formulation, in which particles remain permanently trapped once classified as beached and cannot be re-entrained, even if subsequently re-inundated. This assumption aligns with the benchmark definition and provides a clear endpoint for comparing predicted and observed accumulation patterns. In natural swash environments, however, intermittent re-entrainment can occur, and an absorbing rule may overestimate retention under variable run-up and backwash conditions (Mørk et al., 2026). Consequently, the present predictions should be interpreted as an effective representation of net trapping under controlled experimental conditions rather than a general description of shoreline exchange. Extending the model to include reversible beaching, for instance via event- or state-dependent re-entrainment probabilities, is left for future work.

The present one-way coupling approach also neglects particle feedback on the flow, which may become relevant at high debris concentrations or when buoyant material modifies local momentum exchange or turbulence levels. Extending the framework to two-way coupling regimes would be required to address such conditions.

Finally, several parameters controlling drag, added mass, subgrid-scale dispersion, and beaching are calibrated at the level of material classes to reproduce experimentally observed contrasts in transport and accumulation under a regular wave condition $W2$ (Tables 1 and 3). Although their number could raise concerns about overfitting, these parameters act as proxies for unresolved physical processes that would otherwise require a substantially more complex model. To assess robustness beyond calibration, the calibrated parameter sets are evaluated against an additional regular-wave condition ($W1$). The resulting validation reproduces the main observed trends in transport and accumulation, supporting physical consistency under a second wave forcing (Table 4). Differences observed for buoyant materials under $W1$ suggest sensitivity to certain parameters. Moreover, although $W1$ provides an independent hydrodynamic forcing, it still reflects the same experimental setup and beach geometry used for calibration. Taken together,

these aspects highlight the need for further validation across a wider range of hydrodynamic conditions, including irregular wave forcings and varying beach slopes, to better assess parameter generality and transferability. In this context, the modeling approach aims to identify physically meaningful parameter combinations that reproduce the main transport and accumulation trends, rather than aiming for a universally optimal parameter set.

Overall, the present framework isolates wave-driven hydrodynamics and breaking-induced turbulence as the primary drivers of particle transport and beaching within the benchmark configuration, intentionally omitting processes that may be relevant in real-world settings to better isolate these leading-order controls. The framework should thus be understood as a process-resolving tool to build mechanistic understanding and to derive transferable parametrizations, rather than as a ready-to-use predictive model for arbitrary coastal settings. Extending the approach across hydrodynamic conditions, debris typologies, and coastal morphologies is necessary to develop robust process laws that can be integrated into cost-efficient, larger-scale models, supporting typology-specific predictions of debris accumulation and informing monitoring and mitigation strategies consistent with marine-litter management frameworks, including the EU Marine Strategy Framework Directive.

## 7. Conclusions

In this study, a numerical framework was developed to simulate the transport, dispersion, and accumulation of inertial plastic debris in the surf zone, explicitly accounting for finite-size, non-spherical particles and both buoyant and non-buoyant materials. The approach relies on a one-way CFD–Lagrangian coupling between high-fidelity CFD (OpenFOAM®) to resolve the hydrodynamics and a Lagrangian solver (a modified version of MRE) that incorporates shape- and oscillatory-flow-dependent drag, added mass, stochastic dispersion, and probabilistic beaching. It was calibrated and validated against 2DV wave-flume experiments (Núñez et al., 2023b) for 15 plastic materials spanning contrasting sizes, shapes, and buoyancies.

Validation shows small errors in water levels ($RMSE \approx 0.01$ m, $R^2 > 0.79$) in the pre-breaking and breaking regions and in horizontal velocities ($RMSE \approx 0.02$–$0.10$ m/s, $R^2 > 0.84$) in the same regions, as well as similarly accurate reproduction of debris transport for most materials ($RMSE \approx 0.03$–$0.10\%$, $R^2 > 0.70$), demonstrating robustness across multiple initial conditions. Calibrated parameters reveal clear physical trends: drag decreases with $KC$ (Keulegan–Carpenter number) for oscillatory flow, differentiating large, quasi-steady particles from small materials dominated by oscillatory effects. Added-mass parameters $\beta$ vary systematically with particle size, buoyancy and flexibility, encapsulating complex particle–flow coupling in an effective parameter. Horizontal and vertical dispersion coefficients ($D$) differ by one to two orders of magnitude across zones before and after wave breaking, as well as across buoyancy classes, indicating strongly anisotropic and buoyancy-dependent dispersion, while beaching probabilities remain negligible except for rigid macroplastics that exhibit strong retention in the swash zone.

The framework reproduces key transport pathways and accumulation patterns observed in the experiments, confirming that surf-zone debris dynamics are governed by the coupled effects of wave-breaking hydrodynamics and debris typology. Non-buoyant debris tends to concentrate near the breaking region, whereas buoyant items exhibit size- and geometry-dependent behavior, with smaller debris trapped near the surface and larger sheets intermittently sampling both onshore and offshore-directed flows. These contrasts show that tracer-like assumptions can be insufficient, because typology controls effective depth sampling and the degree of deviation from passive drift, leading to distinct accumulation patterns under identical forcing.

Despite some physically-based model simplifications the framework captures first-order dynamics efficiently. Furthermore, its modularity allows integration with alternative hydrodynamic models, enabling scalable ensemble and scenario analyses. Further research will focus on incorporating second-order mechanisms, refining turbulence–particle interactions, including air–water effects, and extending validation to encompass a broader range of debris typologies, wave conditions, and coastal morphologies. The framework should be understood as a process-resolving tool to derive mechanistic understanding and transferable parametrizations rather than a predictive model for arbitrary settings. Extending its application is essential to develop robust process laws that can be embedded into cost-efficient, larger-scale models, enabling typology-specific predictions of debris accumulation and informing monitoring and mitigation strategies relevant to marine-litter management frameworks.

## Declaration of Generative AI and AI-assisted technologies in the writing process

During the preparation of this work the authors used DeepL Write in order to improve the readability and language of the manuscript. After using this tool, the authors reviewed and edited the content as needed and take full responsibility for the content of the published article.

## CRediT authorship contribution statement

**Paula Núñez:** Writing – review & editing, Writing – original draft, Visualization, Validation, Software, Methodology, Investigation, Funding acquisition, Formal analysis, Data curation, Conceptualization. **Alessandro Romano:** Writing – review & editing, Software, Resources, Methodology, Investigation, Formal analysis, Conceptualization. **Javier L. Lara:** Writing – review & editing, Methodology, Investigation, Conceptualization. **Gabriel Barajas:** Writing – review & editing, Software, Methodology, Investigation. **Raúl Medina:** Writing – review & editing, Methodology, Investigation, Conceptualization. **Giovanni Besio:** Writing – review & editing, Resources, Methodology, Investigation, Conceptualization.

## Acknowledgments

P.N. was supported by a Margarita Salas post-doctoral fellowship funded by European Union-NextGenerationEU, Ministry of Universities and Recovery Transformation and Resilience Plan, through a call from the University of Cantabria. The financial support from the Government of Cantabria through the FÉNIX Program (ID 2020.03.03.322B.742.09) is warmly acknowledged. This research was also partially funded by MICIU/AEI/10.13039/501100011033 through project PID2024-159500OB-I00. Additional support was provided by the "Becas Santander-Investigación Posdoctoral 2025" fellowship program through the University of Cantabria.

## Declaration of competing interest

The authors declare that they have no known competing financial interests or personal relationships that could have appeared to influence the work reported in this paper.

## Appendix. Sensitivity analysis of the hydrodynamic model

This appendix presents a sensitivity analysis of the hydrodynamic model implemented in OpenFOAM®, building on the general setup described in Section 4.1. The analysis focuses on: (i) grid resolution, (ii) near-bed boundary-layer resolution, and (iii) the use of 2D versus 3D wave flume configurations.

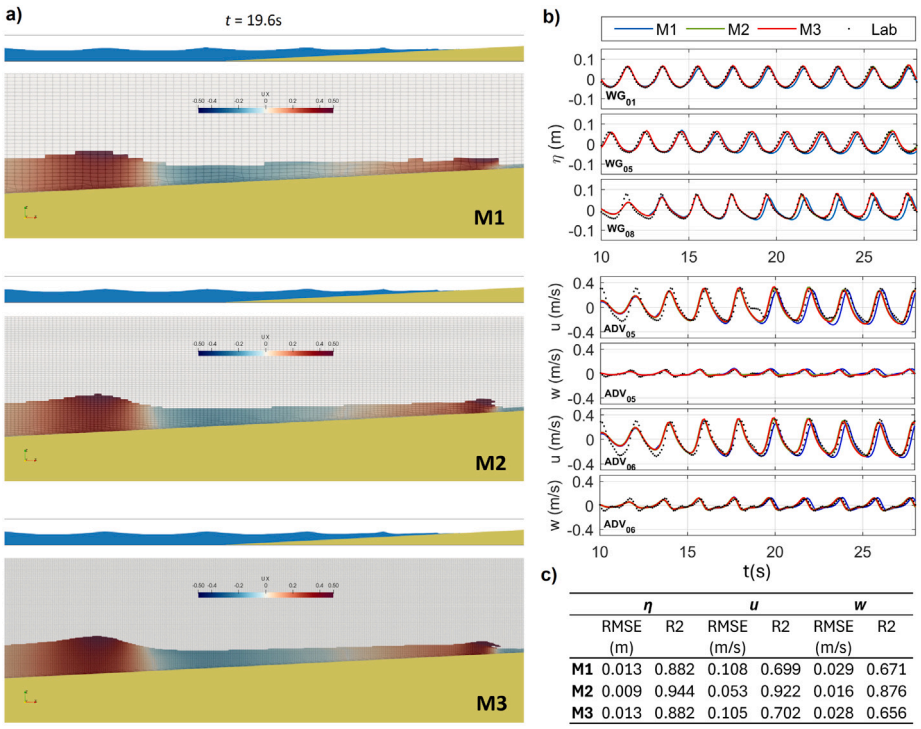


c)

| | η | | u | | w | |
|---|---|---|---|---|---|---|
| | RMSE (m) | R2 | RMSE (m/s) | R2 | RMSE (m/s) | R2 |
| **M1** | 0.013 | 0.882 | 0.108 | 0.699 | 0.029 | 0.671 |
| **M2** | 0.009 | 0.944 | 0.053 | 0.922 | 0.016 | 0.876 |
| **M3** | 0.013 | 0.882 | 0.105 | 0.702 | 0.028 | 0.656 |

**Fig. A.1.** Effect of cell-size discretization on the numerical solution: (a) instantaneous free-surface elevation ($\eta$) and flow velocity at $t$ = 19.6 s for the coarse ($M1$), medium ($M2$), and fine ($M3$) meshes. The upper panel shows the water phase (VoF < 0.5, blue) over the bottom ramp, and the lower panel displays the horizontal velocity magnitude ($u$); (b) time series of $\eta$ at wave gauges $WG_{01}$, $WG_{05}$ and $WG_{08}$, and horizontal ($u$) and vertical ($w$) velocities at $ADV_{05}$ and $ADV_{06}$, for meshes $M1$, $M2$ and $M3$ (colored lines, see legend) compared with laboratory measurements (black markers); and (c) average $RMSE$ and $R^2$ between numerical and experimental data for each variable and mesh at the indicated sensors, computed over ten waves after the initial warming period.

**Table A.1**
Numerical grids used in the sensitivity analysis of grid resolution.

| Mesh name | Discretization | Number of cells |
|---|---|---|
| $M1$ | $\Delta x$ = 0.04 m, $\Delta y$ = 0.01 m, $\Delta z$ = 0.02 m | 0.02M |
| $M2$ | $\Delta x$ = 0.02 m, $\Delta y$ = 0.01 m, $\Delta z$ = 0.01 m | 0.09M |
| $M3$ | $\Delta x$ = 0.01 m, $\Delta y$ = 0.01 m, $\Delta z$ = 0.005 m | 0.35M |

### *A.1. Grid resolution*

A preliminary grid-refinement study was performed to assess the influence of the spatial resolution (both horizontal and vertical) on the hydrodynamic solution. Three unstructured meshes were considered (Table A.1): $M1$ (coarse), $M2$ (medium) and $M3$ (fine), containing approximately 0.02M, 0.09M and 0.35M cells, respectively. The numerical configuration (wave-flume geometry, boundary conditions, wave generation and turbulence model and near-bed surface-layer set-up) is identical to that described in Section 4.1; only the cell size is modified.

Fig. A.1 summarizes the comparison between model results and laboratory data. Free-surface elevation is evaluated at three wave gauges, $WG_{01}$ ($x_1$ = 4.0 m), $WG_{05}$ ($x_2$ = 6.1 m) and $WG_{08}$ ($x_3$ = 11.67 m), while velocity time series are extracted at two positions, $ADV_{05}$ ($x_4$ = 11.67 m, 0.24 m above the bottom) and $ADV_{06}$ ($x_5$ = 13.67 m, 0.31 m above the bottom). Meshes $M2$ and $M3$ provide very similar free-surface and velocity signals, whereas $M1$ exhibits noticeable phase and amplitude discrepancies. These trends are consistent with the statistical indicators ($RMSE$ and $R^2$) reported in the figure, which show a marked improvement from $M1$ to $M2$ (for instance, for $u$, $RMSE$ is reduced by about half and $R^2$ increases from roughly 0.7 to 0.9), whereas $M3$ does not provide any further enhancement and even slightly degrades the agreement for free-surface elevation and velocity components.

From a computational point of view, relative to the coarse mesh ($M1$), the medium mesh ($M2$) is approximately three times more

**Table A.2**
Numerical grids used in the sensitivity analysis of surface-layer configuration.

| Mesh name | Discretization | Surface layers | Number of cells |
|---|---|---|---|
| $MSF1$ | $\Delta x$ = 0.02 m, $\Delta y$ = 0.01 m, $\Delta z$ = 0.01 m | 1 | 0.08M |
| $MSF2$ | $\Delta x$ = 0.02 m, $\Delta y$ = 0.01 m, $\Delta z$ = 0.01 m | 3 | 0.08M |
| $MSF3$ | $\Delta x$ = 0.02 m, $\Delta y$ = 0.01 m, $\Delta z$ = 0.01 m | 6 | 0.09M |
| $MSF4$ | $\Delta x$ = 0.02 m, $\Delta y$ = 0.01 m, $\Delta z$ = 0.01 m | 9 | 0.09M |
| $MSF5$ | $\Delta x$ = 0.02 m, $\Delta y$ = 0.01 m, $\Delta z$ = 0.01 m | 12 | 0.09M |

**Table A.3**
Numerical grids used in the sensitivity analysis of 2D–3D model dimensionality.

| Mesh name | Discretization | Cells in Y direction | Number of cells |
|---|---|---|---|
| $MY1$ | $\Delta x$ = 0.02 m, $\Delta y$ = 0.01 m, $\Delta z$ = 0.01 m | 1 | 0.09M |
| $MY2$ | $\Delta x$ = 0.02 m, $\Delta y$ = 0.01 m, $\Delta z$ = 0.01 m | 5 | 0.45M |
| $MY3$ | $\Delta x$ = 0.02 m, $\Delta y$ = 0.01 m, $\Delta z$ = 0.01 m | 10 | 0.91M |

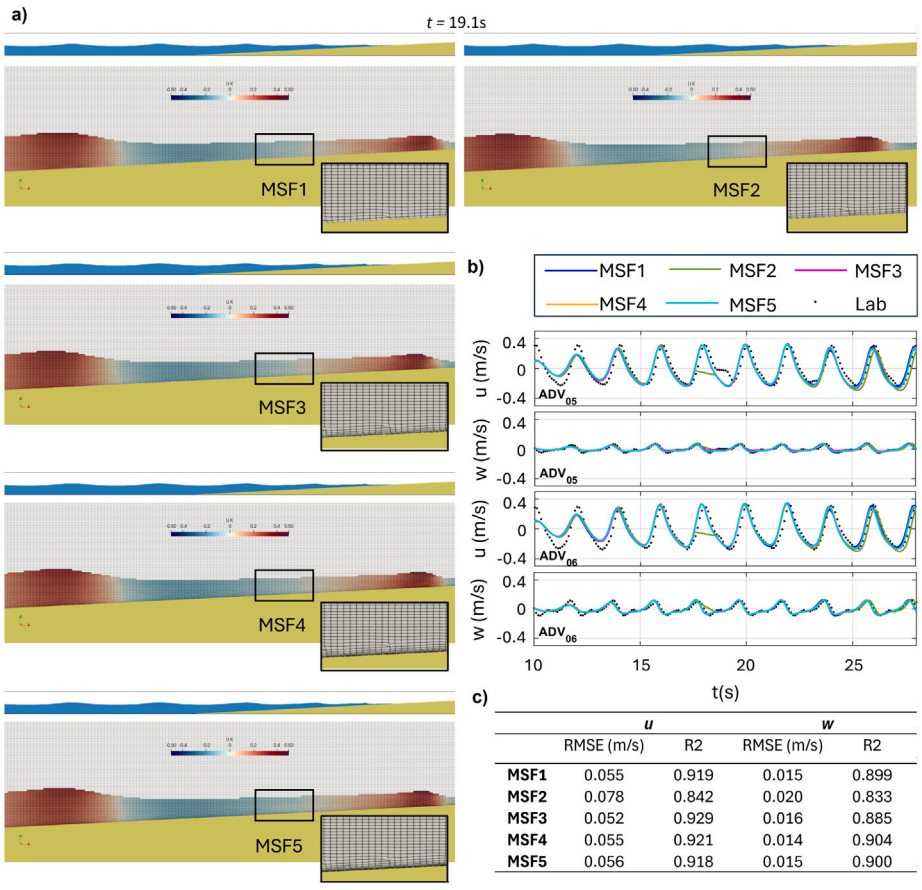


| | u | | w | |
|---|---|---|---|---|
| | RMSE (m/s) | R2 | RMSE (m/s) | R2 |
| **MSF1** | 0.055 | 0.919 | 0.015 | 0.899 |
| **MSF2** | 0.078 | 0.842 | 0.020 | 0.833 |
| **MSF3** | 0.052 | 0.929 | 0.016 | 0.885 |
| **MSF4** | 0.055 | 0.921 | 0.014 | 0.904 |
| **MSF5** | 0.056 | 0.918 | 0.015 | 0.900 |

**Fig. A.2.** Effect of surface-layer refinement on the numerical solution: (a) instantaneous free-surface elevation ($\eta$) and flow velocity at $t = 19.1$s for meshes $MSF1$, $MSF2$, $MSF3$, $MSF4$ and $MSF5$, containing 1, 3, 6, 9, and 12 surface layers, respectively; in each case, the inset highlights the refined near-surface region; (b) time series of horizontal ($u$) and vertical ($w$) velocities at $ADV_{05}$ and $ADV_{06}$ for the five meshes (colored lines, see legend) compared with laboratory measurements (black markers); and (c) average $RMSE$ and $R^2$ at the two ADVs for $u$ and $w$, computed over ten waves after the warming period.

computationally expensive, while the fine mesh ($M3$) increases the cost by nearly an order of magnitude, without commensurate gains in accuracy. Therefore, $M2$ is selected as the reference mesh as it provides the best balance between accuracy and computational efficiency.

### *A.2. Near-bed boundary-layer resolution*

A second set of simulations was carried out to analyze the influence of near-bed surface layers on the hydrodynamic solution. Five meshes were generated (Table A.2) by adding 1, 3, 6, 9, and 12 surface layers at the flume bottom, hereafter denoted $MSF1$–$MSF5$. In all cases, the horizontal and vertical cell sizes away from the bottom coincide with those of mesh $M2$ (Appendix A.1); only the number of surface layers is modified, while the geometry, initial and boundary conditions and numerical parameters are kept identical.

Surface layers follow the local bed slope and concentrate cells in the direction normal to the solid boundary, thereby improving the resolution of the thin shear layer generated by wave breaking over the ramp. Fig. A.2 illustrates the resulting meshes and compares numerical and experimental time series of horizontal and vertical velocities at $ADV_{05}$ and $ADV_{06}$. All configurations reproduce the laboratory signals well, with $RMSE$ in the range 0.052–0.078 m/s for $u$ and between 0.014 and 0.020 m/s for $w$, and $R^2 > 0.84$ for both components. The best overall agreement is obtained for mesh $MSF3$, whereas $MSF2$ shows slightly larger errors and adding more than six surface layers does not lead to any significant improvement.

All five meshes contain a comparable number of cells (approximately 0.08–0.09M) and exhibit similar computational costs. Therefore, considering the slightly better agreement with the laboratory velocity measurements obtained with multiple surface layers, mesh $MSF3$ (six surface layers) is adopted as the reference configuration in the remainder of this study.

### *A.3. 2D vs 3D wave flume configurations*

A final set of simulations was performed to assess the accuracy of representing the experiments with a 2D numerical configuration versus a fully 3D configuration. The main motivation for the 2D approach is the reduction in computational cost, since the dominant dynamics are essentially 2D.

Three meshes were considered (Table A.3), all derived from mesh $MSF3$ (Appendix A.2) and differing only in the number of cells in the spanwise ($y$) direction (and hence in the total number of cells): $MY1$ (2D, one cell in $y$, width 0.01 m, 0.09M cells), $MY2$ (3D, five cells in $y$, width 0.05 m, 0.45M cells) and $MY3$ (3D, ten cells in $y$, width 0.10 m, 0.91M cells).

Fig. A.3 shows the cross-sectional discretization and the comparison between numerical and experimental velocities at $ADV_{05}$ and $ADV_{06}$, sampled at the mid-plane of each flume. All three configurations reproduce the main temporal patterns of horizontal velocity ($u$) and vertical velocity ($w$), but the statistical indicators reveal a progressive degradation of the fit with increasing spanwise extent: for $u$, $RMSE$ increases from 0.053 to 0.140 m/s and $R^2$ decreases from 0.92 to 0.50 between $MY1$ and $MY3$, with similar trends for $w$.

From a computational standpoint, increasing the domain width leads to a substantial rise in computational cost. The longer wall-clock

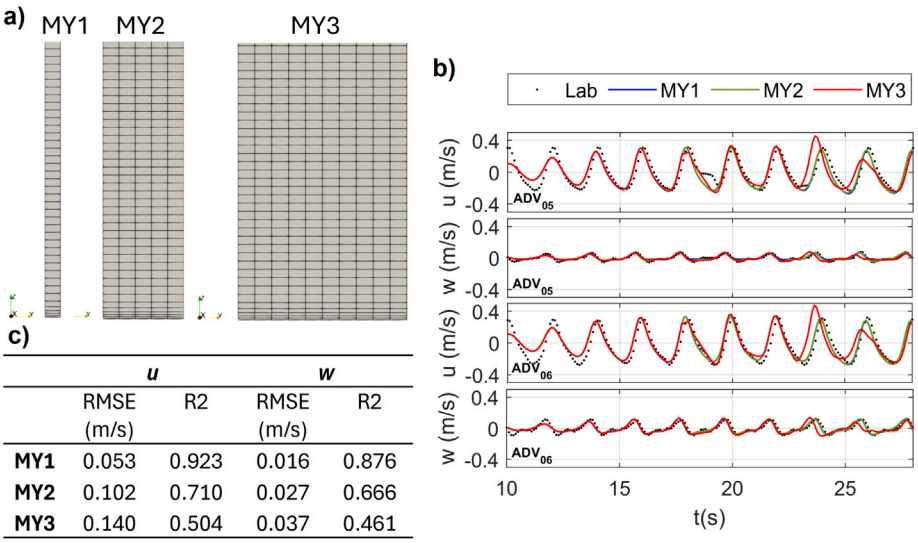


c)

| | u | | w | |
|---|---|---|---|---|
| | RMSE (m/s) | R2 | RMSE (m/s) | R2 |
| **MY1** | 0.053 | 0.923 | 0.016 | 0.876 |
| **MY2** | 0.102 | 0.710 | 0.027 | 0.666 |
| **MY3** | 0.140 | 0.504 | 0.037 | 0.461 |

**Fig. A.3.** Effect of transverse setup on the numerical solution: (a) mesh configurations $MY1$ (2D), $MY2$ (3D) and $MY3$ (3D) with increasing width in the spanwise ($y$) direction; (b) time series of horizontal ($u$) and vertical ($w$) velocities at $ADV_{05}$ and $ADV_{06}$ for the three meshes (colored lines, see legend) compared with laboratory measurements (black markers); and (c) average $RMSE$ and $R^2$ between numerical and experimental data for $u$ and $w$ at the two ADVs, computed over ten waves after the warming period.

times observed for ($MY2$) and ($MY3$) compared to ($MY1$), even when using more processors, are attributable to both the increased cell count and reduced parallel efficiency. Accordingly, the 2D mesh ($MY1$) is selected as the most suitable configuration when balancing accuracy and efficiency.

## Data availability

Data will be made available on request.

## References


Alletto, M., Breuer, M., 2012. One-way, two-way and four-way coupled LES predictions of a particle-laden turbulent flow at high mass loading downstream of a confined bluff body. Int. J. Multiph. Flow 45, 70–90.

Alsina, J.M., Jongedijk, C.E., van Sebille, E., 2020. Laboratory measurements of the wave-induced motion of plastic particles: Influence of wave period, plastic size and plastic density. J. Geophys. Res.: Ocean. 125, e2020JC016294.

Barnes, D.K., Galgani, F., Thompson, R.C., Barlaz, M., 2009. Accumulation and fragmentation of plastic debris in global environments. Phil. Trans. R. Soc. B 364, 1985–1998.

Berrouk, A., Laurence, D., Riley, J., Stock, D., 2007. Stochastic modelling of inertial particle dispersion by subgrid motion for LES of high Reynolds number pipe flow. J. Turbul. N50.

Boi, S., 2019. Exact results on the large-scale stochastic transport of inertial particles including the basset history term. Phys. Fluids 31.

Boi, S., Afonso, M.M., Mazzino, A., 2015. Anomalous diffusion of inertial particles in random parallel flows: Theory and numerics face to face. J. Stat. Mech. Theory Exp. 2015, P10023.

Brackbill, J.U., Kothe, D.B., Zemach, C., 1992. A continuum method for modeling surface tension. J. Comput. Phys. 100, 335–354.

Brown, S.A., Greaves, D.M., Magar, V., Conley, D.C., 2016. Evaluation of turbulence closure models under spilling and plunging breakers in the surf zone. Coast. Eng. 114, 177–193.

Calvert, R., Peytavin, A., Pham, Y., Duhamel, A., van der Zanden, J., van Essen, S., Sainte-Rose, B., van den Bremer, T., 2024. A laboratory study of the effects of size, density, and shape on the wave-induced transport of floating marine litter. J. Geophys. Res.: Ocean. 129, e2023JC020661.

Cardoso, C., Caldeira, R.M.A., 2021. Modeling the exposure of the Macaronesia Islands (NE Atlantic) to marine plastic pollution. Front. Mar. Sci. 8, 653502.

Carlson, D.F., Suaria, G., Aliani, S., Fredj, E., Fortibuoni, T., Griffa, A., Russo, A., Melli, V., 2017. Combining litter observations with a regional ocean model to identify sources and sinks of floating debris in a semi-enclosed basin: The Adriatic Sea. Front. Mar. Sci. 4, 78.

Chella, M.A., Bihs, H., Myrhaug, D., Muskulus, M., 2015. Breaking characteristics and geometric properties of spilling breakers over slopes. Coast. Eng. 95, 4–19.

Chen, Z., Bowen, M., Li, G., Coco, G., Hall, B., 2022. Retention and dispersion of buoyant plastic debris in a well-mixed estuary from drifter observations. Marine Poll. Bull. 180, 113793.

Christensen, E.D., 2006. Large eddy simulation of spilling and plunging breakers. Coast. Eng. 53, 463–485.

Christensen, E.D., Deigaard, R., 2001. Large eddy simulation of breaking waves. Coast. Eng. 42, 53–86.

Critchell, K., Grech, A., Schlaefer, J., Andutta, F.P., Lambrechts, J., Wolanski, E., Hamann, M., 2015. Modelling the fate of marine debris along a complex shoreline: Lessons from the Great Barrier Reef. Estuar. Coast. Shelf Sci. 167, 414–426.

De Leo, A., Cutroneo, L., Sous, D., Stocchino, A., 2021. Settling velocity of microplastics exposed to wave action. J. Mar. Sci. Eng. 9, 142.

De Leo, A., Stocchino, A., 2022. Dispersion of heavy particles under sea waves. Phys. Fluids 34.

Declerck, A., Delpey, M., Rubio, A., Ferrer, L., Basurko, O.C., Mader, J., Louzao, M., 2019. Transport of floating marine litter in the coastal area of the south-eastern Bay of Biscay: A Lagrangian approach using modelling and observations. J. Oper. Ocean. 12, S111–S125.

Dehbi, A., 2008. Turbulent particle dispersion in arbitrary wall-bounded geometries: A coupled CFD-Langevin-equation based approach. Int. J. Multiph. Flow 34, 819–828.

Deike, L., Melville, W.K., Popinet, S., 2016. Air entrainment and bubble statistics in breaking waves. J. Fluid Mech. 801, 91–129.

Derakhti, M., Kirby, J.T., Shi, F., Ma, G., 2016a. Wave breaking in the surf zone and deep-water in a non-hydrostatic RANS model. Part 1: Organized wave motions. Ocean. Model. 107, 125–138.

Derakhti, M., Kirby, J.T., Shi, F., Ma, G., 2016b. Wave breaking in the surf zone and deep-water in a non-hydrostatic RANS model. Part 2: Turbulence and mean circulation. Ocean. Model. 107, 139–150.

Derraik, J.G., 2002. The pollution of the marine environment by plastic debris: a review. Marine Poll. Bull. 44, 842–852.

Devolder, B., Troch, P., Rauwoens, P., 2018. Performance of a buoyancy-modified $k-\omega$ and $k-\omega$ SST turbulence model for simulating wave breaking under regular waves using OpenFOAM®. Coast. Eng. 138, 49–65.

Di Paolo, B., Lara, J.L., Barajas, G., Losada, Í.J., 2021. Wave and structure interaction using multi-domain couplings for Navier-Stokes solvers in OpenFOAM®. Part I: Implementation and validation. Coast. Eng. 164, 103799.

Díaz, B., Pavón, A., Gómez-Gesteira, M., 2008. Use of a probabilistic particle tracking model to simulate the Prestige oil spill. J. Mar. Syst. 72, 159–166.

DiBenedetto, M.H., Clark, L.K., Pujara, N., 2022. Enhanced settling and dispersion of inertial particles in surface waves. J. Fluid Mech. 936, A38.

DiBenedetto, M.H., Ouellette, N.T., Koseff, J.R., 2018. Transport of anisotropic particles under waves. J. Fluid Mech. 837, 320–340.

Drossinos, Y., Reeks, M.W., 2005. Brownian motion of finite-inertia particles in a simple shear flow. Phys. Rev. E 71, 031113.

Eaton, J.K., 2009. Two-way coupled turbulence simulations of gas-particle flows using point-particle tracking. Int. J. Multiph. Flow 35, 792–800.

Forsberg, P.L., Sous, D., Stocchino, A., Chemin, R., 2020. Behaviour of plastic litter in nearshore waters: First insights from wind and wave laboratory experiments. Marine Poll. Bull. 153, 111023.

Galgani, F., Hanke, G., Maes, T., 2015. Global distribution, composition and abundance of marine litter. Mar. Anthr. Litter 29–56.
Gatignol, R., 1983. The Faxén formulae for a rigid particle in an unsteady non-uniform Stokes flow.
Ghosh, A., Suara, K., McCue, S.W., Yu, Y., Soomere, T., Brown, R.J., 2021. Persistency of debris accumulation in tidal estuaries using Lagrangian coherent structures. Sci. Total Environ. 781, 146808.
Gorman, D., Gutierrez, A.R., Turra, A., Manzano, A.B., Balthazar-Silva, D., Oliveira, N.R., Harari, J., 2020. Predicting the dispersal and accumulation of microplastic pellets within the estuarine and coastal waters of South-Eastern Brazil using integrated rainfall data and Lagrangian particle tracking models. Front. Environ. Sci. 8, 559405.
Guler, H.G., Larsen, B.E., Quintana, O., Goral, K.D., Carstensen, S., Christensen, E.D., Kerpen, N.B., Schlurmann, T., Fuhrman, D.R., 2022. Experimental study of non-buoyant microplastic transport beneath breaking irregular waves on a live sediment bed. Marine Poll. Bull. 181, 113902.
Hardesty, B.D., Harari, J., Isobe, A., Lebreton, L., Maximenko, N., Potemra, J., Van Sebille, E., Vethaak, A.D., Wilcox, C., 2017. Using numerical model simulations to improve the understanding of micro-plastic distribution and pathways in the marine environment. Front. Mar. Sci. 4, 240234.
Higuera, P., Lara, J.L., Losada, I.J., 2013a. Realistic wave generation and active wave absorption for Navier-Stokes models: Application to OpenFOAM®. Coast. Eng. 71, 102–118.
Higuera, P., Lara, J.L., Losada, I.J., 2013b. Simulating coastal engineering processes with OpenFOAM®. Coast. Eng. 71, 119–134.
Hölzer, A., Sommerfeld, M., 2008. New simple correlation formula for the drag coefficient of non-spherical particles. Powder Technol. 184, 361–365.
Iuppa, C., Passalacqua, G., Faraci, C., 2024. An equilibrium criterion for plastic debris fate in wave-driven transport. Marine Poll. Bull. 206, 116758.
Jalón-Rojas, I., Sous, D., Marieu, V., 2025. A wave-resolving two-dimensional vertical Lagrangian approach to model microplastic transport in nearshore waters based on TrackMPD 3.0. Geosci. Model. Dev. 18, 319–336.
Jalón-Rojas, I., Wang, X.H., Fredj, E., 2019. A 3D numerical model to track marine plastic debris (TrackMPD): Sensitivity of microplastic trajectories and fates to particle dynamical properties and physical processes. Marine Poll. Bull. 141, 256–272.
Jasak, H., 1996. Error analysis and estimation in the finite volume method with applications to fluid flows.
Kako, S., Isobe, A., Kataoka, T., Hinata, H., 2014. A decadal prediction of the quantity of plastic marine debris littered on beaches of the East Asian marginal seas. Marine Poll. Bull. 81, 174–184.
Kako, S., Isobe, A., Magome, S., Hinata, H., Seino, S., Kojima, A., 2011. Establishment of numerical beach-litter hindcast/forecast models: An application to Goto Islands, Japan. Marine Poll. Bull. 62, 293–302.
Kerpen, N.B., Schlurmann, T., Schendel, A., Gundlach, J., Marquard, D., Hüpgen, M., 2020. Wave-induced distribution of microplastic in the surf zone. Front. Mar. Sci. 7, 590565.
Klink, D., Peytavin, A., Lebreton, L., 2022. Size dependent transport of floating plastics modeled in the global ocean. Front. Mar. Sci. 9, 903134.
Kolahdouz, E.M., Bhalla, A.P.S., Scotten, L.N., Craven, B.A., Griffith, B.E., 2021. A sharp interface Lagrangian-Eulerian method for rigid-body fluid-structure interaction. J. Comput. Phys. 443, 110442.
Larsen, B.E., Al-Obaidi, M.A.A., Guler, H.G., Carstensen, S., Goral, K.D., Christensen, E.D., Kerpen, N.B., Schlurmann, T., Fuhrman, D.R., 2023. Experimental investigation on the nearshore transport of buoyant microplastic particles. Marine Poll. Bull. 187, 114610.
Larsen, B.E., Fuhrman, D.R., 2018. On the over-production of turbulence beneath surface waves in Reynolds-averaged Navier–Stokes models. J. Fluid Mech. 853, 419–460.
Law, K.L., Morét-Ferguson, S., Maximenko, N.A., Proskurowski, G., Peacock, E.E., Hafner, J., Reddy, C.M., 2010. Plastic accumulation in the North Atlantic subtropical gyre. Science 329, 1185–1188.
Lebreton, L.M., Greer, S., Borrero, J.C., 2012. Numerical modelling of floating debris in the world's oceans. Marine Poll. Bull. 64, 653–661.
Legates, D.R., McCabe, G.J., 1999. Evaluating the use of "goodness-of-fit" measures in hydrologic and hydroclimatic model validation. Water Resour. Res. 35, 233–241.
Li, G., Chen, Z., Bowen, M., Coco, G., 2024. Transport and retention of sinking microplastics in a well-mixed estuary. Marine Poll. Bull. 203, 116417.
Li, Y., Larsen, B.E., Fuhrman, D.R., 2022. Reynolds stress turbulence modelling of surf zone breaking waves. J. Fluid Mech. 937, A7.
Marschall, H., Hinterberger, K., Schüler, C., Habla, F., Hinrichsen, O., 2012. Numerical simulation of species transfer across fluid interfaces in free-surface flows using OpenFOAM. Chem. Eng. Sci. 78, 111–127.
Maxey, M.R., Riley, J.J., 1983. Equation of motion for a small rigid sphere in a nonuniform flow. Phys. Fluids 26 (4), 883–889.
Mørk, J.M., Nordam, T., Leirvik, F., Mostaani, A., Nepstad, R., Stevenson-Jones, R., Kleven, A., Breivik, Å®, 2026. A Lagrangian model of wave-induced beaching and resuspension of plastic particles. Marine Poll. Bull. 222, 118718.
Nayak, A.R., McFarland, M.N., Sullivan, J.M., Twardowski, M.S., 2018. Evidence for ubiquitous preferential particle orientation in representative oceanic shear flows. Limnol. Oceanogr. 63, 122–143.
Núñez, P., Castanedo, S., Medina, R., 2020. A global classification of astronomical tide asymmetry and periodicity using statistical and cluster analysis. J. Geophys. Res.: Ocean. 125, e2020JC016143.
Núñez, P., Castanedo, S., Medina, R., 2021. Role of ocean tidal asymmetry and estuarine geometry in the fate of plastic debris from ocean sources within tidal estuaries. Estuar. Coast. Shelf Sci. 259, 107470.
Núñez, P., García, A., Mazarrasa, I., Juanes, J.A., Abascal, A.J., Méndez, F., Castanedo, S., Medina, R., 2019. A methodology to assess the probability of marine litter accumulation in estuaries. Marine Poll. Bull. 144, 309–324.
Núñez, P., Misic, C., Cutroneo, L., Capello, M., Medina, R., Besio, G., 2023a. Biofilm-induced effect on the buoyancy of plastic debris: An experimental study. Marine Poll. Bull. 193, 115239.
Núñez, P., Pérez-García, L., Rezaee, S.M., Bárcena, J.F., García, A., 2025. Experimental study of buoyant macro-and mesoplastic trapping by Spartina maritima. Marine Poll. Bull. 216, 118005.
Núñez, P., Romano, A., García-Alba, J., Besio, G., Medina, R., 2023b. Wave-induced cross-shore distribution of different densities, shapes, and sizes of plastic debris in coastal environments: A laboratory experiment. Marine Poll. Bull. 187, 114561.
Olascoaga, M.J., Beron-Vera, F.J., Miron, P., Triñanes, J., Putman, N., Lumpkin, R., Goni, G., 2020. Observation and quantification of inertial effects on the drift of floating objects at the ocean surface. Phys. Fluids 32.
Rahmani, A., Stocchino, A., 2026. Eulerian–Lagrangian simulation of wave-induced microplastic dispersion in nearshore zones: Processes and implications. Estuar. Coast. Shelf Sci. 328, 109626.
Raimundo, G.I., Sousa, M.C., Dias, J.M., 2020. Numerical modelling of plastic debris transport and accumulation throughout Portuguese coast. J. Coast. Res. 95, 1252–1257.
Reeks, M., 1988. The relationship between brownian motion and the random motion of small particles in a turbulent flow. Phys. Fluids 31, 1314–1316.
Ruiz, I., AJ, A., Basurko, O.C., Rubio, A., 2022. Modelling the distribution of fishing-related floating marine litter within the Bay of Biscay and its marine protected areas. Environ. Pollut. 292, 118216.
Sánchez-González, J.F., Sánchez-Rojas, V., Memos, C.D., 2011. Wave attenuation due to posidonia oceanica meadows. J. Hydraul. Res. 49, 503–514.
Santamaria, F., Boffetta, G., Afonso, M.M., Mazzino, A., Onorato, M., Pugliese, D., 2013. Stokes drift for inertial particles transported by water waves. Europhys. Lett. 102, 14003.
Sarpkaya, T., 1986. Force on a circular cylinder in viscous oscillatory flow at low Keulegan–Carpenter numbers. J. Fluid Mech. 165, 61–71.
Schmaltz, E., Melvin, E.C., Diana, Z., Gunady, E.F., Rittschof, D., Somarelli, J.A., Virdin, J., Dunphy-Daly, M.M., 2020. Plastic pollution solutions: emerging technologies to prevent and collect marine plastic pollution. Environ. Int. 144, 106067.
Stocchino, A., De Leo, F., Besio, G., 2019. Sea waves transport of inertial micro-plastics: Mathematical model and applications. J. Mar. Sci. Eng. 7, 467.
Suara, K., Khanarmuei, M., Brown, R., 2020. Quantification of inertial effect on the transport of macro-plastics in a tidal embayment. In: Proceedings of the 22nd Australasian Fluid Mechanics Conference. AFMC2020, The University of Queensland.
Tang, Y., Guo, B., Ranjan, D., 2015. Numerical simulation of aerosol deposition from turbulent flows using three-dimensional RANS and LES turbulence models. Eng. Appl. Comput. Fluid Mech. 9, 174–186.
Van Sebille, E., England, M.H., Froyland, G., 2012. Origin, dynamics and evolution of ocean garbage patches from observed surface drifters. Environ. Res. Lett. 7, 044040.
Van Sebille, E., Griffies, S.M., Abernathey, R., Adams, T.P., Berloff, P., Biastoch, A., Blanke, B., Chassignet, E.P., Cheng, Y., Cotter, C.J., et al., 2018. Lagrangian ocean analysis: Fundamentals and practices. Ocean. Model. 121, 49–75.
Villarrubia-Gómez, P., Cornell, S.E., Fabres, J., 2018. Marine plastic pollution as a planetary boundary threat- The drifting piece in the sustainability puzzle. Mar. Policy 96, 213–220.
Wang, Z., Yang, J., Stern, F., 2016. High-fidelity simulations of bubble, droplet and spray formation in breaking waves. J. Fluid Mech. 792, 307–327.
Weller, H.G., 2008. A New Approach to VOF-Based Interface Capturing Methods for Incompressible and Compressible Flow, vol. 4, OpenCFD Ltd., p. 35, Report TR/HGW 1647.
Willmott, C.J., 1981. On the validation of models. Phys. Geogr. 2, 184–194.
Zambianchi, E., Iermano, I., Suaria, G., Aliani, S., 2014. Marine litter in the Mediterranean Sea: an oceanographic perspective. In: Marine Litter in the Mediterranean and Black Seas CIESM Workshop Monograph. CIESM Publisher, pp. 31–41.
Zambianchi, E., Trani, M., Falco, P., 2017. Lagrangian transport of marine litter in the Mediterranean Sea. Front. Environ. Sci. 5, 5.
Zhang, H., 2017. Transport of microplastics in coastal seas. Estuar. Coast. Shelf Sci. 199, 74–86.
Zhou, Z., Hsu, T.J., Cox, D., Liu, X., 2017. Large-eddy simulation of wave-breaking induced turbulent coherent structures and suspended sediment transport on a barred beach. J. Geophys. Res.: Ocean. 122, 207–235.